

A multi-adenylate cyclase regulator at the flagellar tip controls African trypanosome transmission

Sabine Bachmaier

Ludwig-Maximilians-Universität München (LMU) <https://orcid.org/0000-0001-7416-8613>

Giacomo Giacomelli

Ludwig-Maximilians-Universität München (LMU)

Estéfania Calvo-Alvarez

Institut Pasteur, Université de Paris

Larissa Rezende Vieira

Federal University of Rio de Janeiro <https://orcid.org/0000-0003-1596-3953>

Jan Van Den Abbeele

Institute of Tropical Medicine <https://orcid.org/0000-0002-4533-4480>

Aris Aristodemou

Ludwig-Maximilians-Universität München (LMU) <https://orcid.org/0000-0002-3266-4499>

Esben Lorentzen

Aarhus University

Matthew Gould

Ludwig-Maximilians-Universität München (LMU)

Ana Brennand

Ludwig-Maximilians-Universität München (LMU)

Jean-Wiliam Dupuy

University of Bordeaux <https://orcid.org/0000-0002-2448-4797>

Ignasi Forné

Iudwig-Maximilians-University Munich (LMU)

Axel imhof

BioMedical center <https://orcid.org/0000-0003-2993-8249>

Marc Bramkamp

Kiel University <https://orcid.org/0000-0002-7704-3266>

Didier Salmon

Federal University of Rio de Janeiro

Brice Rotureau

Institut Pasteur

Michael Boshart (✉ boshart@lmu.de)

Ludwig-Maximilians-Universität München (LMU) <https://orcid.org/0000-0002-5070-2663>

Article

Keywords:

Posted Date: January 25th, 2022

DOI: <https://doi.org/10.21203/rs.3.rs-1216579/v1>

License:  This work is licensed under a Creative Commons Attribution 4.0 International License.

[Read Full License](#)

Version of Record: A version of this preprint was published at Nature Communications on September 16th, 2022. See the published version at <https://doi.org/10.1038/s41467-022-33108-z>.

1 **A multi-adenylate cyclase regulator at the flagellar tip controls African**
2 **trypanosome transmission**

3

4 Sabine Bachmaier^{1*}, Giacomo Giacomelli^{2#}, Estéfania Calvo-Alvarez^{3#}, Larissa
5 Rezende Vieira⁴, Jan Van Den Abbeele⁵, Aris Aristodemou¹, Esben Lorentzen⁶,
6 Matt K. Gould¹, Ana Brennand¹, Jean-Wiliam Dupuy⁷, Ignasi Forné⁸, Axel
7 Imhof⁸, Marc Bramkamp², Didier Salmon⁴, Brice Rotureau³, Michael Boshart^{1*}

8

9 ¹ *Faculty of Biology, Genetics, Ludwig-Maximilians-University Munich (LMU),*
10 *82152 Martinsried, Germany*

11 ² *Faculty of Biology, Microbiology, Ludwig-Maximilians-University Munich*
12 *(LMU), 82152 Martinsried and Institute for General Microbiology, Kiel*
13 *University, 24118 Kiel, Germany*

14 ³ *Institut Pasteur, Université de Paris, INSERM U1201, Trypanosome Cell*
15 *Biology Unit, Trypanosome Transmission Group, 75015 Paris, France*

16 ⁴ *Institute of Medical Biochemistry Leopoldo de Meis, Centro de Ciências e*
17 *da Saúde, Federal University of Rio de Janeiro, Av. Brigadeiro Trompowski,*
18 *Rio de Janeiro 21941-590, Brazil*

19 ⁵ *Trypanosoma Unit, Department of Biomedical Sciences, Institute of Tropical*
20 *Medicine Antwerp, 2000 Antwerp, Belgium*

21 ⁶ *Department of Molecular Biology and Genetics, Aarhus University, Gustav*
22 *Wieds Vej 10c, 8000 Aarhus C, Denmark*

23 ⁷ *Univ. Bordeaux, Plateforme Protéome, 33000 Bordeaux, France*

24 ⁸ Biomedical Center, Ludwig-Maximilians-University Munich, 82152

25 Martinsried, Germany

26

27 # authors equally contributed

28 * corresponding authors:

29 Sabine Bachmaier

30 sabine.bachmaier@lrz.uni-muenchen.de, Tel.: 49-89-2180-74600

31 Michael Boshart

32 boshart@lmu.de, Tel.: 49-89-2180-74600

33 **Abstract**

34 Signaling from ciliary nanodomains controls developmental processes in
35 metazoans. Trypanosome transmission requires development and migration
36 in the tsetse vector alimentary tract. Flagellar cAMP signaling has been linked
37 to parasite social motility (SoMo) *in vitro*, yet uncovering control of directed
38 migration in fly organs is challenging. Here we show that the architecture of
39 an adenylate cyclase (AC) complex in the flagellar tip nanodomain is essential
40 for tsetse salivary gland (SG) colonization and SoMo. Cyclic AMP response
41 protein 3 (CARP3) binds and regulates multiple AC isoforms. CARP3 tip
42 localization depends on the scaffold FLAM8. Re-localization of CARP3 away
43 from the tip nanodomain is sufficient to abolish SoMo and fly SG colonization.
44 Since intrinsic development is normal in $\Delta carp3$ and $\Delta flam8$ mutant parasites,
45 AC complex-mediated tip signaling specifically controls parasite migration and
46 thereby transmission. Participation of several developmentally regulated
47 receptor-type AC isoforms may indicate the complexity of the *in vivo* signals
48 perceived.

49 **Introduction**

50 All cells perceive their environment and signal outside information to control
51 adaptive and developmental processes. For parasites, perception of the host
52 environment by physical and chemical cues is essential for survival and
53 transmission. Digenetic parasites face challenging rapid changes of biotic
54 environments between their reservoir and vector hosts¹. Pathways processing
55 extracellular signals are not conserved in phylogenetically distant
56 kinetoplastids, including *Trypanosoma*^{2,3}, and the connection of identified
57 signaling components remains to be solved. Trypanosomes shuttle between
58 mammalian and insect hosts and are well-studied due to medical and
59 economic impact as causative agents of neglected tropical diseases in
60 humans and animals⁴. A phenotype termed social motility (SoMo)⁵, a process
61 similar to bacterial swarming⁶, indicates intercellular communication or peer
62 signaling in populations of unicellular trypanosomes. On semisolid surfaces,
63 cultured procyclic insect forms of *T. brucei* migrate away from an initial
64 inoculation point by radial swarming⁵. Cyclic adenosine monophosphate
65 (cAMP) is key for control of SoMo⁷⁻⁹. Individual flagellar tip localized members
66 of a large multigene family of transmembrane receptor-type adenylyl cyclases
67 (ACs) are involved in the process⁷. Swarm-like collective motion of
68 trypanosomes in different tsetse tissues and organs has been observed^{10,11},
69 yet its relation to SoMo *in vitro* is unclear. A common mechanism for SoMo
70 and directed migration in the tsetse midgut has been suggested based on
71 correlated phenotypes upon deletion of *PDEB1*⁹.

72 Similar to the flagellum of mammalian sperm¹², the trypanosome's single
73 flagellum represents a cAMP signaling compartment, as it displays a strong
74 enrichment of ACs and phosphodiesterases (PDEs), ubiquitous enzymes
75 producing or degrading cAMP, respectively. The trypanosome flagellar tip is a
76 site with particular importance for interaction with host tissue surfaces¹³ and
77 forms a distinct microdomain. This is defined by exclusive localization of a
78 subset of flagellar proteins¹⁴⁻¹⁷, including some members of the AC multigene
79 family¹⁸. The cAMP microdomain concept was first described by Buxton and
80 Brunton¹⁹ and is now well established in different systems²⁰ including primary
81 cilia^{21,22}. The high spatiotemporal specificity of cAMP signaling within these
82 micro- or nanodomains depends on signaling cascades with sensor proteins,
83 transducers and effectors often arranged as multiprotein complexes, or
84 signalosomes, that can include scaffolding proteins such as AKAPs (A kinase
85 anchoring proteins). Localized PDEs limit the diffusion of the second
86 messenger and can generate cAMP concentration gradients across a cell,
87 while PDE inhibition has been shown to result in loss of cAMP
88 compartmentalization²³. Within the very small cAMP nanodomains (~50-100
89 nm), extremely high local cAMP concentrations are possible that can
90 specifically regulate even low affinity effectors located within the nanodomain.
91 Virtually nothing is known about cyclase regulation or downstream cAMP
92 signaling in kinetoplastids. These organisms lack known cyclase activators,
93 such as G protein-coupled receptors (GPCRs) and known cAMP effectors
94 including cAMP-dependent PKA²⁴ or cyclic nucleotide-gated ion channels²⁵.
95 The large family of receptor-type ACs with an extracellular N-terminal domain

96 was suggested to provide the diversity for reception of multiple signals,
97 although no ligands of these ACs have been identified to date²⁶. In
98 bloodstream form (BSF) parasites that infect the mammalian host,
99 disturbance of the intracellular cAMP concentration is critical for growth and
100 cytokinesis²⁷⁻²⁹. Exploiting this phenotype, a genome-wide RNAi screen for
101 cAMP resistance identified cAMP response proteins (CARPs) as candidates
102 for novel cAMP effectors or pathway modulators in *T. brucei*³⁰. Among these,
103 CARP3 is a trypanosome-specific protein.

104 AC activity plays an important role in innate immunity subversion of
105 bloodstream stage trypanosomes early in infection³¹, The most abundant AC
106 involved is encoded by subtelomeric polycistronic transcription units driving
107 bloodstream form-specific variant surface glycoprotein expression (VSG
108 expression sites)³², hence named expression site-associated gene 4
109 (ESAG4). Trypanosomes shuttle between the bloodstream and tissues of a
110 mammalian host and the alimentary tract and salivary glands of a tsetse fly
111 undergoing a series of developmental transitions that result in defined
112 adapted stages³³. Cyclic AMP signaling was suggested to play a role in stage
113 development due to differential expression of transcripts encoding AC
114 isoforms in trypanosomes colonizing midgut, proventriculus or salivary glands,
115 respectively^{34,35}. During their complex journey through the insect vector,
116 trypanosomes are in intimate contact with host tissue surfaces and have to
117 cope with several bottlenecks³⁶.

118 Here, we provide direct evidence that a cAMP signalosome is essential for
119 trypanosome migration in the tsetse vector. Perturbation of the architecture of

120 an AC complex at the flagellar tip is alone sufficient to abolish SoMo and
121 tsetse salivary gland colonization. The mutant parasites retain full intrinsic
122 developmental competence. The highly specific phenotype elicited by the
123 trypanosome-specific AC regulator CARP3 will stimulate further dissection of
124 novel mechanisms of cAMP signaling.

125

126

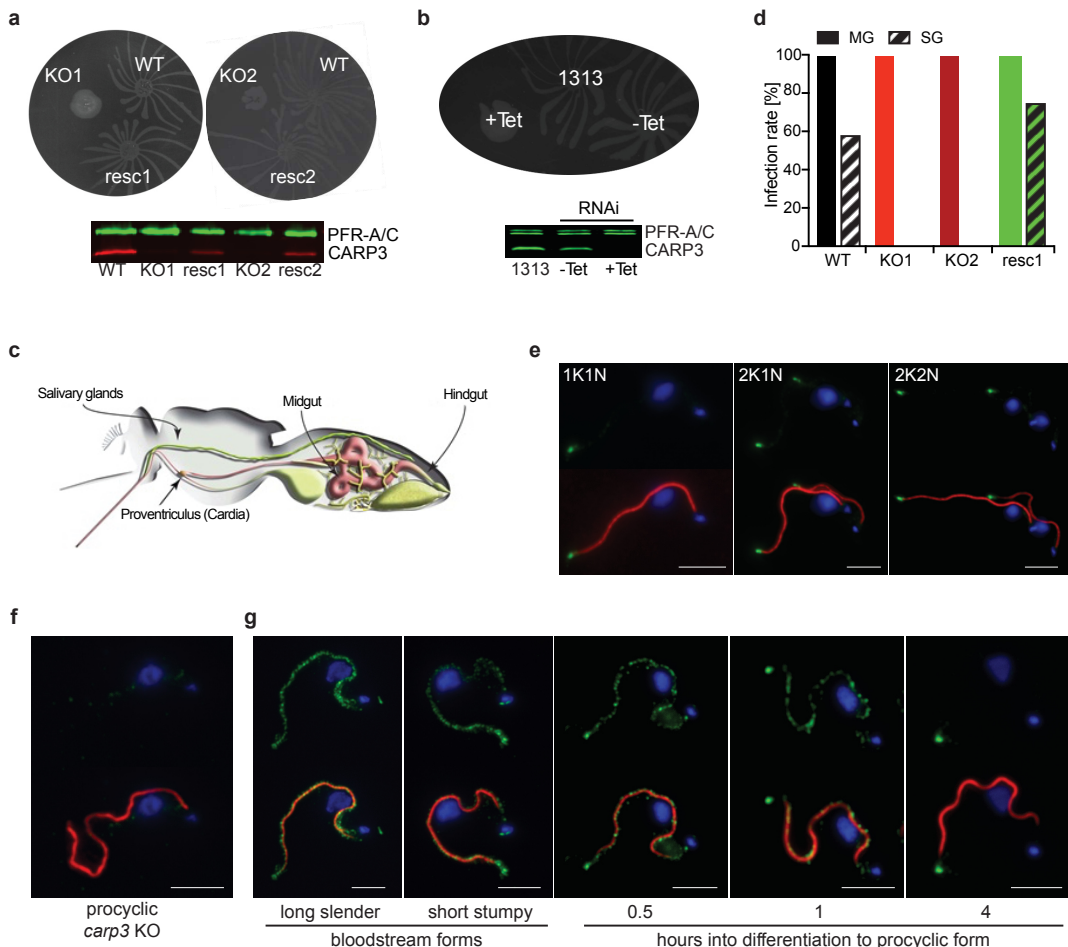
127 **Results**

128

129 **CARP3 is a flagellar tip protein essential for social motility and**
130 **colonization of tsetse fly salivary glands**

131 We previously identified the cAMP response protein CARP3 in an RNAi
132 screen for cAMP resistance in bloodstream forms (BSFs) of *T. brucei*³⁰.
133 CARP3 is a protein with no sequence homology outside *Trypanosoma* and
134 unknown biochemical functions, except N-terminal myristylation site(s)
135 (<http://lipid.biocuckoo.org/webserver.php>). Its novel predicted structure
136 (AlphaFold2³⁷) is shown in Extended Data Fig. 1a. As cAMP regulates social
137 motility (SoMo) in procyclic forms (PCFs)^{8,38}, we asked whether CARP3 did
138 also control the parasite's colonization of the tsetse fly vector. A homozygous
139 *CARP3* deletion mutant, its endogenous single allele *CARP3* rescue, as well
140 as a tetracycline-inducible *CARP3* RNAi cell line were generated in the fully
141 differentiation-competent pleomorphic *T. brucei* strain AnTat 1.1 'Munich'³⁹
142 and analyzed for *in vitro* culture phenotypes in SoMo, single cell motility,
143 growth and differentiation. Deletion or depletion of *CARP3* caused a complete
144 block in SoMo (Fig. 1a,b). In contrast, single cell mean velocity in viscous
145 medium, growth of freshly differentiated PCFs and BSFs and development of

146 slender to stumpy BSFs and further to PCFs were all unaffected (Extended
147 Data Fig. 1b-g). The journey of trypanosomes in the tsetse fly vector proceeds
148 through additional well-defined developmental stages. The parasites migrate
149 from the insect's midgut via the cardia (proventriculus) to the salivary glands
150 (SGs) (Fig. 1c). Upon ingestion of stumpy BSFs by tsetse flies, *carp3* KO cells
151 were unable to colonize the SGs, while showing high midgut infection rates
152 (Fig. 1d). The single-allele *CARP3* rescue was sufficient to restore SG
153 infection rates to wild type levels. Indirect immunofluorescence analysis using
154 a CARP3-specific polyclonal antibody revealed localization of CARP3 to the
155 flagellar tip in PCFs (Fig. 1e, Extended Data Fig. 1h), consistent with
156 subcellular proteome studies^{16,17,40}. CARP3 is concentrated at the tip of the
157 parental and daughter flagella (Fig. 1e) and it appears close to the flagellar
158 membrane as a horseshoe-shaped signal with a slight anterior to posterior
159 gradient (Extended Data Fig. 1h). No signal was detected in the *carp3* KO cell
160 line (Fig. 1f). Surprisingly, in BSFs, CARP3 localized along the entire length of
161 the flagellum and at the posterior cell pole (Fig. 1g, Extended Data Fig. 1i)
162 with subcellular redistribution within the first hours of BSF to PCF
163 differentiation. This dynamic localization of CARP3 during parasite
164 development may correlate with life-cycle stage-specific functions. In PCFs,
165 immunofluorescence analysis also suggested colocalization of CARP3 and
166 Ty1-tagged adenylate cyclase isoforms ACP1 or ACP6 at the flagellar tip (Fig.
167 2a).



168

169 **Fig. 1** CARP3 is a flagellar tip regulator of social motility (SoMo) and is essential for colonization
170 of tsetse fly salivary glands.

171 **a**, SoMo assays of procyclic *T. brucei* AnTat 1.1 wild type (WT), *carp3* knock out (KO, two independent
172 clones KO1, KO2) or *in situ* *CARP3* rescue (resc, two independent clones resc1, resc2). The Western
173 blot for WT, KO1 and resc1 was probed with anti-CARP3 and anti-PFR-A/C (loading control).

174 **b**, SoMo assay upon tetracycline (Tet)-inducible RNAi of *CARP3* (-Tet / +Tet 24h) and the parental
175 *AnTat 1.1* 1313 cell line. The Western blot shows *CARP3* repression detected by antibodies as in (a).

176 **c**, Illustration of the digestive system and the salivary glands of a tsetse fly (adapted from⁴¹).

177 **d**, Infection rates of tsetse fly midgut (MG) or salivary glands (SG) with *T. brucei* AnTat 1.1 cell lines as
178 in (a). Flies were dissected 34-36 days p.i., n (flies) = 48 (WT), 50 (KO1), 50 (KO2), 40 (resc1). 10 mM
179 L-glutathione was included in the blood meal.

180 **e, f**, Indirect immunofluorescence analysis of *CARP3* (green) in *T. brucei* AnTat 1.1 procyclic form WT
181 (e) or *carp3* KO (f). The upper panels show *CARP3* (green) and the nuclear and mitochondrial DNA
182 stained with DAPI (blue), the lower panels show an overlay with the axoneme (red; stained with the
183 antibody mAB25). In (e) cells in different cell cycle stages are shown (1K1N, 2K1N, 2K2N; K kinetoplast,
184 N nucleus).

185 **g**, Indirect immunofluorescence analysis of *CARP3* (green) as in (e, f) during culture differentiation from
186 bloodstream to procyclic forms. Scale bar in (e-g) 5 μm.

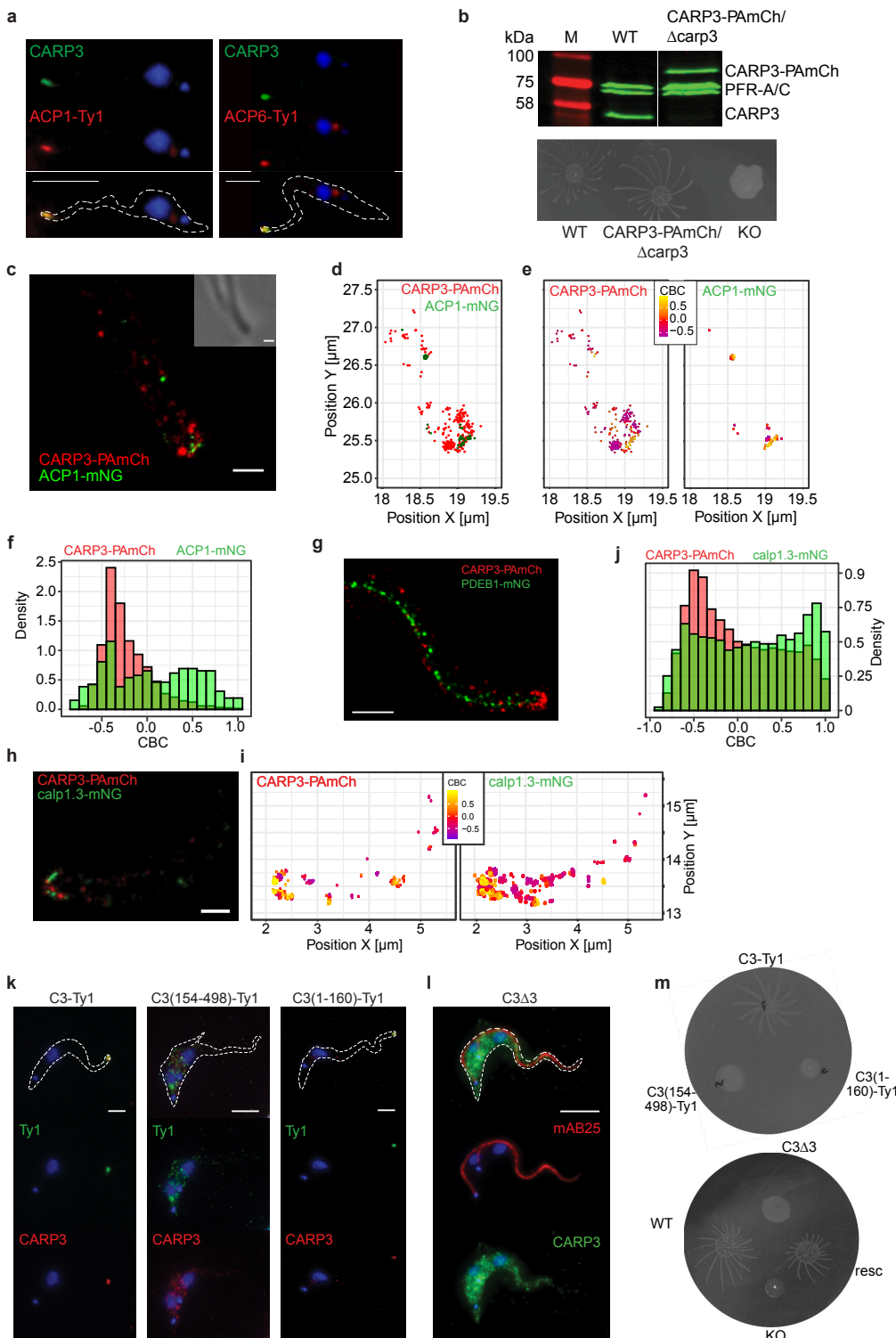
187

188 **Super-resolved spatial correlation of CARP3 with components of SoMo**
189 **signaling**

190 To precisely localize components of cAMP signaling involved in SoMo in the
191 tip microdomain, we used photo-activated localization microscopy (PALM) for
192 CARP3, ACP1 and phosphodiesterase PDEB1. One allele of *CARP3* was C-
193 terminally fused *in situ* to photo-activatable mCherry (CARP3-PAmCherry).
194 The fusion protein was fully functional in SoMo, as deletion of the wild type
195 *CARP3* allele in the transgenic line did not impair SoMo on agarose plates
196 (Fig. 2b). Quantitative colocalization analysis at single molecule resolution
197 was used to detect distinct subdomains at the flagellar tip (radius ~ 300 nm).
198 This confirmed close proximity of CARP3 to the flagellar tip membrane (Fig.
199 2c). In the same cell line, ACP1 was C-terminally fused *in situ* to
200 mNeonGreen (ACP1-mNG) (Extended Data Fig. 2a). ACP1-mNG localized to
201 the flagellar tip membrane (Fig. 2c and Extended Data Fig. 2b) as expected
202 from the presence of a transmembrane domain (TMD) and consistent with
203 previous reports^{17,18}. The probability of colocalization between two
204 fluorescently tagged protein populations was determined by the coordinate-
205 based colocalization (CBC) analysis method of Malkusch, et al.⁴² (details see
206 methods). As positive control, we generated a cell line with one *CARP3* allele
207 fused to PAmCherry and the other *CARP3* allele fused to mNeonGreen
208 (Extended Data Fig. 2c). The CBC values' distribution for non-colocalizing
209 proteins (negative control) was instead obtained by simulating two
210 independent Poisson point patterns (Extended Data Fig. 2f and 3, see

211 methods for details). Comparison of the CBC values' distribution of CARP3-
212 PAmCherry and ACP1-mNG (23.46% events with $\text{CBC} \geq 0.5$) with the
213 negative control (2.19% of events with $\text{CBC} \geq 0.5$, see Supplementary Table
214 1) showed significant colocalization for CARP3-ACP1 ($p < 0.05$) that was in
215 the same range as the positive control (CARP3-PAmCherry-CARP3mNG;
216 22.22% events with $\text{CBC} \geq 0.5$, see Supplementary Table 1). CBC values
217 higher than 0.5 can be generally observed at the extreme tip of the flagellum
218 (Fig. 2d-f).

219 PDEB1 was also C-terminally fused to mNeonGreen and expressed in the
220 CARP3-PAmCherry line (Extended Data Fig. 2a). Live cell fluorescence
221 microscopy shows localization of PDEB1-mNG along the flagellum in a tip to
222 base decreasing gradient (Extended Data Fig. 2b). At single molecule
223 resolution, PDEB1-mNG does not localize to the far anterior tip of the
224 trypanosome flagellum, in agreement with previous localization to the
225 paraflagellar rod (Fig. 2g)^{8,28,40}.



226

227 **Fig. 2 Super-resolution topology in the flagellar tip nanodomain.**

228 **a**, Indirect immunofluorescence analysis of CARP3 (green) and the adenylate cyclases ACP1 (left) or
229 ACP6 (right), respectively, fused to a C-terminal Ty1 epitope tag (anti-Ty1, red) in procyclic *T. brucei* 29-
230 13. DNA was stained with DAPI (blue). Upper panels: CARP3 + DNA; middle panels: ACP1-Ty1 or
231 ACP6-Ty1 + DNA; lower panels: merge of all three channels. Scale bars 5 μm.

232 **b**, Western blot analysis (top) and SoMo assay (bottom) of a procyclic *T. brucei* AnTat 1.1E CARP3-
233 PAmCherry/Δcarp3 cell line. Wild type (WT) and homozygous *carp3* knock out (KO) cells were included
234 as controls. The Western blot was probed with anti-CARP3 and anti-PFR-A/C (loading control). M:
235 protein molecular weight marker.

236 **c**, PALM imaging of CARP3-PAmCherry (PAmCh, red) and ACP1-mNeonGreen (mNG, green) at the
237 flagellar tip of procyclic *T. brucei* AnTat 1.1E. Corresponding phase contrast shown as inset. Scale bars
238 0.5 μm.

239 **d**, Single molecule localization from (c) is shown via centroids. CARP3-PAmCherry is displayed in red,
240 ACP1-mNeonGreen in green.

241 **e, f**, Colocalization analysis of CARP3-PAmCherry with ACP1-mNeonGreen. CARP3 (**e**, left) and ACP1
242 (**e**, right) localizations are color coded according to their respective Coordinate Based Colocalization
243 values (CBC), where a higher CBC value signifies a higher likelihood of colocalization. CBC histograms
244 (**f**) of CARP3-PAmCherry (red) and ACP1-mNeonGreen (green) single molecule distributions. The
245 overlay of red and green bars is shown in dark green. All CBC values were calculated in a maximum
246 radius of 300 nm and radius intervals of 5 nm. n = 19 flagella.

247 **g**, PALM imaging of CARP3-PAmCherry (red) and PDEB1-mNeonGreen (green) in the flagellum of
248 procyclic *T. brucei* AnTat 1.1E. Scale bar 0.5 μm.

249 **h-j**, PALM imaging (**h**) and colocalization analysis (**i, j**) of CARP3-PAmCherry (red) and calpain 1.3-
250 mNG (green) at the flagellar tip of procyclic *T. brucei* AnTat 1.1E. CARP3 (**i**, left) and calpain 1.3 (**i**,
251 right) localizations are color coded according to their respective CBC values. Scale bar 0.5 μm.
252 Quantification in (**j**) shows CBC histograms of CARP3-PAmCherry (red) and calpain 1.3-mNG (green)
253 single-molecule distributions. The overlay of red and green bars is shown in dark green. n = 15 flagella.

254 **k, l**, Indirect immunofluorescence analysis of CARP3 localization in procyclic *T. brucei* AnTat 1.1 upon
255 constitutive overexpression of CARP3-Ty1, CARP3(154-489)-Ty1 or CARP3(1-160)-Ty1 or in situ add-
256 back of *CARP3Δ3* in a *carp3* knock out background. (**k**) Anti-CARP3 red, anti-Ty1 green, DAPI (DNA)
257 blue. (**l**) mAB25 (anti-TbSAXO) red, anti-CARP3 green. Scale bars 5 μm.

258 **m**, SoMo assay of cell lines as in (**k, l**) including WT and *carp3* KO.

259

260 **The N-terminus of CARP3 is essential for flagellar tip membrane**

261 **localization and SoMo**

262 In absence of a predicted transmembrane domain, membrane-proximal
263 localization of CARP3 suggests interaction with membrane(-associated)
264 proteins or (dual) acylation^{43,44}. In order to position CARP3 relative to the
265 membrane at single-molecule resolution, we co-expressed CARP3-
266 PAmCherry with an mNeonGreen fusion of the previously characterized
267 flagellar tip protein calpain 1.3 (Fig. 2h; Extended Data Fig. 2a) that is

268 associated with the membrane via N-terminal dual acylation¹⁴. The CBC
269 values' distribution for the CARP3-PAmCherry / calpain 1.3-mNG combination
270 (Fig. 2i,j) showed significant colocalization with 33.9% of events with CBC \geq
271 0.5, while the negative control remained at 2.19% ($p < 0.05$) and the positive
272 control (CARP3-PAmCherry-CARP3mNG) at 22.22% (Supplementary Table 1
273 and Extended Data Fig. 2e,f and 3). CARP3 was found in a chemical
274 proteomic survey of myristoylated proteins⁴⁵ in addition to the sequence
275 prediction of myristylation. The structural model of CARP3, computed using
276 AlphaFold³⁷, shows a highly structured α -helical domain predicted with high
277 confidence and interspaced by several long loops that are predicted with low
278 confidence and likely represent intrinsically disordered (ID) regions (Extended
279 Data Fig. 1a). To define the domain responsible for localization, deletion
280 mutants of CARP3 were expressed in a *carp3* knock out background
281 (Extended Data Fig. 4a). Upon removal of the N-terminal 153 amino acids, C-
282 terminally Ty1-tagged CARP3 was no longer localized at the flagellar tip,
283 whereas expression of CARP3(1-160)-Ty1 was sufficient for flagellar tip
284 targeting (Fig. 2k). CARP3(1-160)-Ty1 seems to be unstable as its expression
285 level is too low for detection by Western blot (Extended Data Fig. 4a) but
286 sufficient for detection by IFA (Fig. 2k). Upon deletion of the three N-terminal
287 glycine residues (CARP3 Δ 3 mutant), no CARP3 was detected at the flagellar
288 tip (Fig. 2l). The expression level of CARP3 Δ 3 was comparable to that of full-
289 length CARP3 (Extended Data Fig. 4b). The deletion analysis strongly
290 supports an essential role of myristylation as well as sufficiency of the N-
291 terminal structured domain for tip localization. Strikingly, all cell lines devoid of

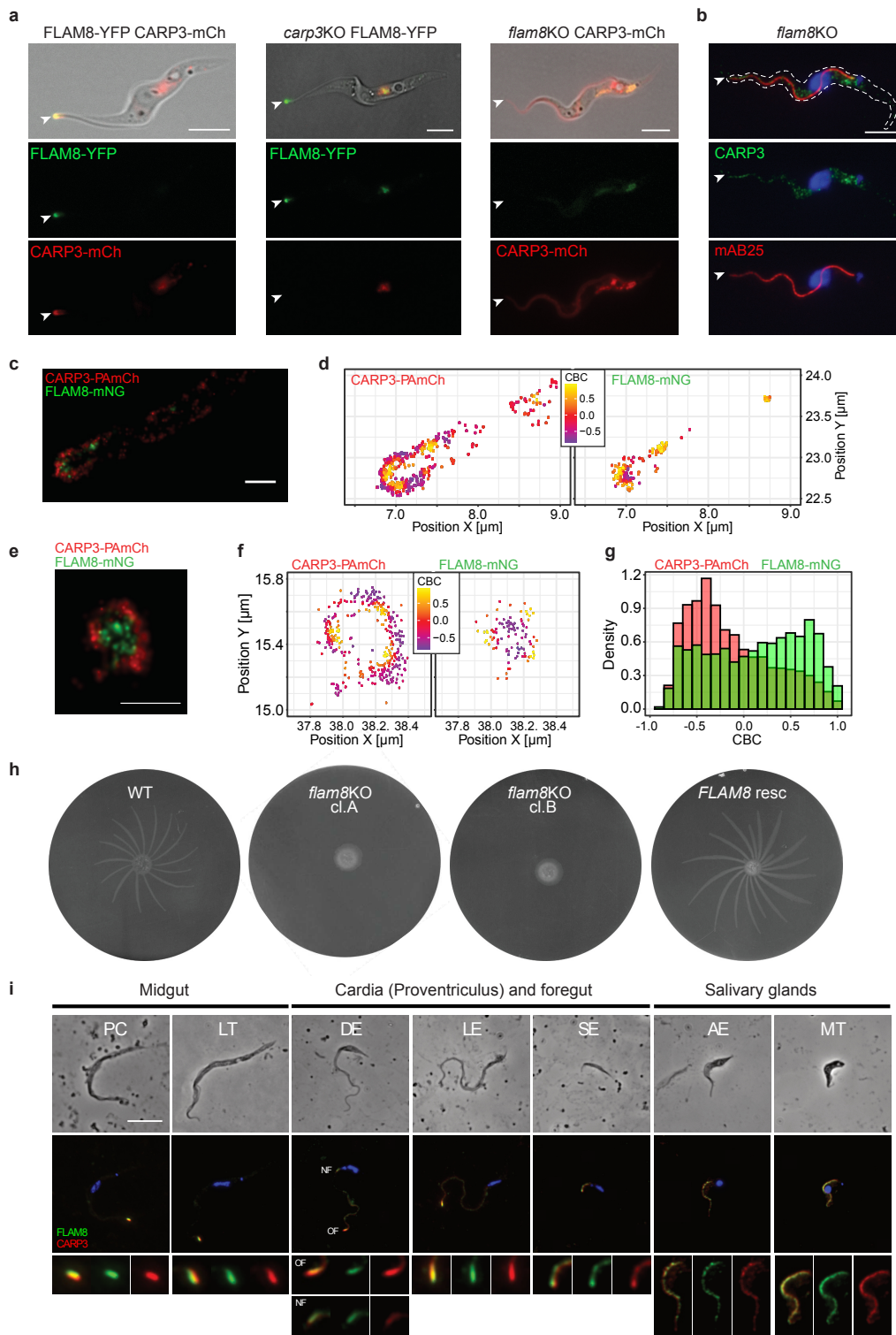
292 CARP3 at the flagellar tip were deficient in SoMo (Fig. 2m). We thus conclude
293 that the precise localization of CARP3 at the flagellar tip is critical for
294 trypanosome SoMo. The SoMo deficiency of the C-terminal CARP3 deletion
295 mutant (CARP3(1-160)-Ty1) is not informative due to very low expression
296 (Fig. 2m; Extended Data Fig. 4a).

297

298 **FLAM8 is required for flagellar tip localization of CARP3**

299 To define the extension of the CARP3 containing microdomain, colocalization
300 with FLAM8 (Flagellar Member 8) was tested. FLAM8 is a large cytoskeletal
301 flagellar tip protein proposed to localize at the plus end of the axonemal
302 microtubules in PCFs¹⁵. FLAM8 was C-terminally fused *in situ* to either YFP
303 (FLAM8-YFP)¹⁵ or mNeonGreen (FLAM8-mNG) and expressed in PCF
304 CARP3-mCherry or CARP3-PAmCherry cells, respectively (Extended Data
305 Fig. 2a,b). Whereas wide field fluorescence microscopy showed the expected
306 tip localization of both CARP3-mCherry and FLAM8-YFP (Fig. 3a), at single-
307 molecule resolution, distinct zones for CARP3-PAmCherry and FLAM8-mNG
308 were identified (Fig. 3c-f; Extended Data Fig. 5c). FLAM8 was found in the tip
309 interior compared to the membrane-proximal CARP3 in flagellar longitudinal
310 (Fig. 3c,d) and flagellar tip cross-sections (Fig. 3e,f). In a flagellar tip cross-
311 section with a radius of approximately 300 nm, the two proteins were
312 characterized by a colocalization interface in a zone ranging between 150 and
313 200 nm from the center (Extended Data Fig. 5c). The CBC values' distribution
314 for the CARP3-PAmCherry / FLAM8-mNG combination shows 30.14% of
315 events with CBC ≥ 0.5 compared to 2.19% for the negative control (Fig. 3g,

316 Extended Data Fig. 2f, Supplementary Table 1). This significant difference (p
317 < 0.05) is consistent with an association of a fraction of CARP3 with FLAM8 at
318 the proposed localization of FLAM8 at the plus end of the axonemal
319 microtubules¹⁵. Thus, separate pools of CARP3 seem to exist and FLAM8
320 might be involved in tip accumulation of CARP3. To test this hypothesis,
321 CARP3-mCherry was expressed in the $\Delta flam8$ homozygous deletion
322 background⁴⁶. Homogenous distributions of CARP3-mCherry (Fig. 3a) and
323 endogenous CARP3 (Fig. 3b) were seen along the length of the flagellum as
324 well as in the cytoplasm. In contrast, localization of FLAM8-YFP remained
325 unchanged in a *carp3* knock out cell line (Fig. 3a). Given the essential role of
326 FLAM8 for the tip localization of CARP3, the SoMo deficiency of $\Delta flam8$ cells
327 was not surprising (Fig. 3h). Controls verified that $\Delta flam8$ cells had single cell
328 motility and growth properties comparable to the parental cell line (Extended
329 Data Fig. 5a,b). Also, adding back a single *FLAM8* allele fully restored wild
330 type SoMo (Fig. 3h). In summary, these data show that FLAM8 is essential for
331 tip localization of CARP3 and that delocalization of CARP3 is sufficient to
332 produce the SoMo-deficient phenotype.



333

334 **Fig. 3 FLAM8 is essential for flagellar tip localization of CARP3 and for SoMo.**

335 a, Live cell fluorescence microscopy of procyclic *T. brucei* AnTat 1.1E expressing FLAM8-YFP (green)
 336 and CARP3-mCherry (CARP3-mCh, red) (left), AnTat 1.1 carp3 KO cells expressing FLAM8-YFP
 337 (center) or AnTat 1.1E flam8 KO cells expressing CARP3-mCherry in (right). Top: merge of fluorescent
 338 channels with DIC; middle: YFP; bottom: mCherry.

339 **b**, Indirect immunofluorescence analysis of CARP3 (green) in procyclic *T. brucei* AnTat 1.1E *flam8* KO
340 cells. DNA was stained with DAPI (blue), the axoneme is labeled in red (detected by the antibody
341 mAB25). Top: merge of fluorescent channels; middle: CARP3+DAPI; bottom: mAB25+DAPI. White
342 arrowheads in (a) and (b) point towards flagellar tips; scale bars 5 μ m.
343 **c, d**, PALM imaging (**c**) and colocalization analysis (**d**) of CARP3-PAmCherry (PAmCh) and FLAM8-
344 mNeonGreen (mNG) at the flagellar tip of procyclic *T. brucei* AnTat 1.1. CARP3 (d, left) and FLAM8 (d,
345 right) localizations are color coded according to their respective CBC values.
346 **e**, PALM imaging of CARP3-PAmCherry (PAmCh) and FLAM8-mNeonGreen (mNG) at a cross-section
347 of the flagellar tip of procyclic *T. brucei* AnTat 1.1. Scale bars in (c) and (e) are 0.5 μ m.
348 **f**, Colocalization analysis as in (d) for a flagellar tip cross section.
349 **g**, CBC histograms of CARP3-PAmCherry (red) and FLAM8-mNG (green) single molecule distributions
350 calculated from the data shown in panels (c-f). The overlay of red and green bars is shown in dark
351 green. n = 27 flagella.
352 **h**, SoMo assay of procyclic *T. brucei* AnTat 1.1E wild type (WT), *flam8* KO (two subclones: A, B) or *in*
353 *situ* *FLAM8* rescue (resc) cells expressing a fluorescent triple marker.
354 **i**, Distribution of CARP3 and FLAM8 during the parasite cycle in the tsetse fly. Immunofluorescence on
355 methanol-fixed trypanosomes obtained from dissected tsetse tissues four weeks after infection. Anti-
356 CARP3 (red), anti-FLAM8 (green), DAPI (blue). Flagellum regions in white boxes on bright field are
357 magnified in the bottom panel. Scale bar 5 μ m. PC procyclic; LT long mesocyclic trypomastigote; DE
358 dividing epimastigote; LE long epimastigote; SE short epimastigote; AE attached epimastigote; MT
359 metacyclic; OF old flagellum; NF new flagellum.

360
361 Proximity of CARP3 and FLAM8 was observed in all developmental stages of
362 trypanosomes isolated from different tsetse fly alimentary tract compartments
363 and salivary glands (Fig. 3i). The flagellar tip colocalization found in midgut
364 (procyclic and long trypomastigotes) and cardiac stages (dividing and long
365 epimastigotes) was contrasting to the redistribution of both proteins along the
366 length of the flagellum in short epimastigotes in the cardia as well as in
367 attached epimastigotes and mammalian-infective metacyclic forms in the
368 tsetse salivary glands. The CARP3 localization pattern in salivary gland
369 stages was similar to that in bloodstream forms (Fig. 1g, Extended Data Fig.
370 1i). The dynamic localization of FLAM8 and CARP3 in the life cycle suggests

371 a specific functional role at the flagellar tip in the parasite stages migrating in
372 the fly's alimentary tract.

373

374 **Transmission-deficient trypanosomes are developmentally competent**

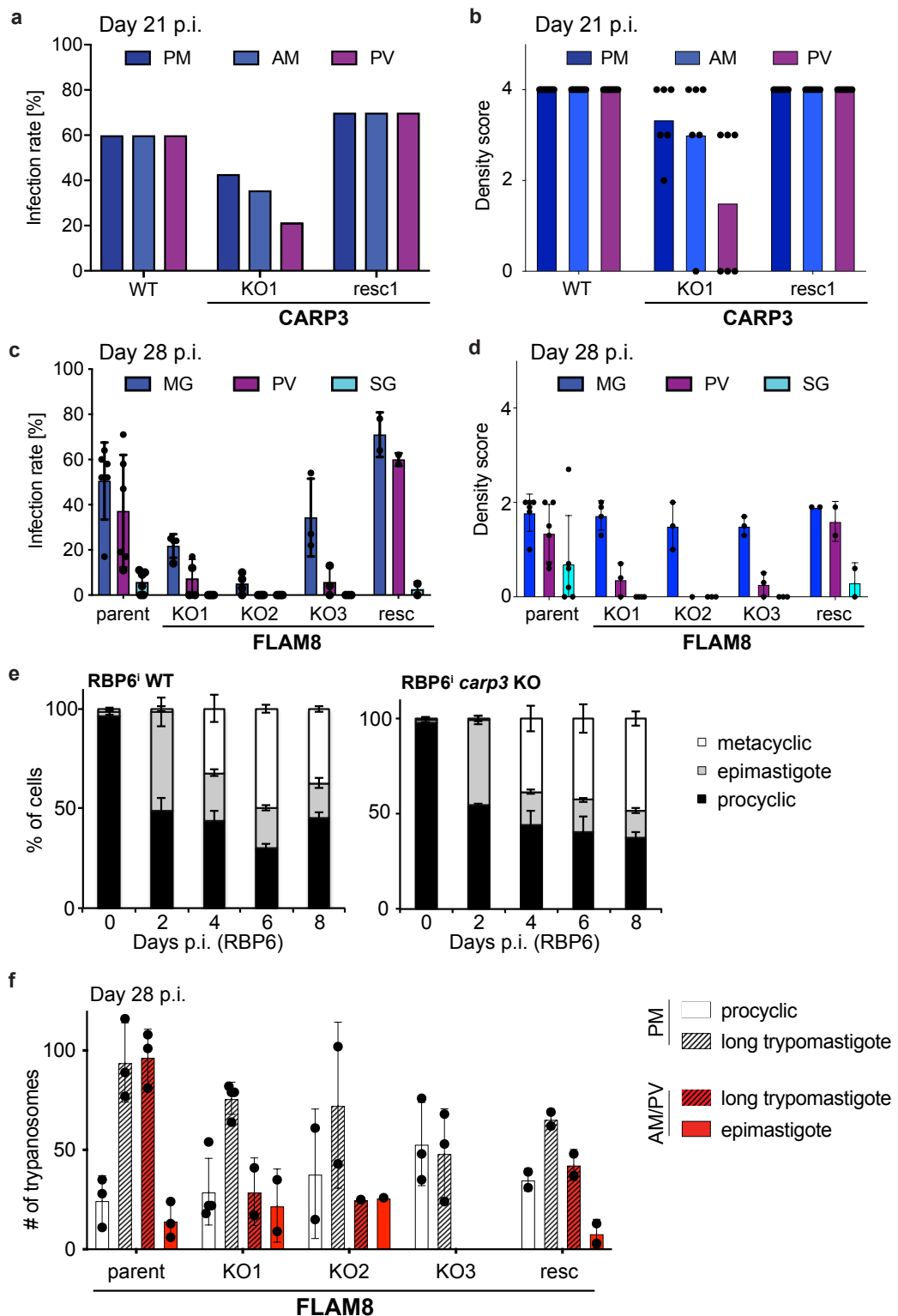
375 We then tested the ability of $\Delta carp3$ and $\Delta flam8$ parasites to colonize tsetse
376 salivary glands and asked the crucial question whether the phenotypes were
377 due to migration or to an intrinsic developmental defect. Both mutants were
378 able to colonize the tsetse cardia, albeit with lower observed parasite

379 densities and at a reduced rate as compared to wild type cells (Fig. 4a-d).

380 Midgut infection rates were barely affected for $\Delta carp3$ (Fig. 1d, Fig. 4a) and
381 reduced for $\Delta flam8$ (Fig. 4c), respectively. The key finding is that not a single
382 mutant trypanosome reached the salivary glands in any of the 355 flies
383 dissected (100 flies infected with $\Delta carp3$, Fig. 1d; 255 flies infected with
384 $\Delta flam8$, Fig. 4c) in contrast to wild type parasites or rescued lines. Thus,
385 *CARP3* and *FLAM8* represent two genes that impact both SoMo and vector
386 colonization when deleted.

387 To check the impact of *CARP3* deletion on the intrinsic developmental
388 competence of the parasite, we differentiated $\Delta carp3$ parasites in culture
389 using inducible overexpression of the post-transcriptional regulator RBP6⁴⁸.
390 RBP6 overexpression was induced in wild type and $\Delta carp3$ parasites
391 (Extended Data Fig. 6), and followed by morphological analysis (Fig. 4e) and
392 stage-specific marker expression profiling (Extended Data Fig. 6d). Efficiency
393 and kinetics of differentiation from the procyclic form, via the epimastigote
394 morphotype, to the metacyclic stage was identical for wild type cells and

395 $\Delta carp3$ cells. Similarly, development of $\Delta flam8$ parasites was analyzed *in vivo*
396 by imaging the parasites at different time points during their cyclical
397 development in the fly (Fig. 4f). Procyclic forms and long trypomastigotes
398 (mesocyclics) were found in the tsetse posterior midgut, and long
399 trypomastigotes and epimastigotes in the anterior midgut and cardia, showing
400 that these developmental stages are formed and viable in the absence of
401 FLAM8, hence in the absence of tip-localized CARP3. However, the number
402 of long trypomastigotes in the anterior midgut and cardia was reduced in
403 $\Delta flam8$ parasites as compared to WT, suggesting that long trypomastigote
404 parasites may be impaired in migration to or colonization of the anterior
405 midgut and/or cardia. These results exclude a defect in the intrinsic
406 developmental potential of the mutant trypanosomes and argue that the
407 strong salivary gland colonization phenotype is specifically due to a sensory
408 or signaling defect at the flagellar tip, possibly in long trypomastigotes,
409 impinging on forward migration in the tsetse fly digestive tract.



410

411 **Fig. 4** *Carp3* and *flam8* KO parasites are developmentally competent but show reduced infection
412 of tsetse fly organs.

413 **a**, Infection rates and **b**, parasite densities in posterior midgut (PM), anterior midgut (AM) or
414 proventriculus (PV or cardia) of tsetse flies infected with *T. brucei* AnTat 1.1 wild type (WT), *carp3* knock
415 out (KO1) or *in situ* *CARP3* rescue (resc1) cells (Institute of Tropical Medicine Antwerp tsetse fly

416 colony). Flies were dissected 21 days p.i. n (flies) = 15 (WT), 14 (KO1), 10 (resc1). Parasite densities
417 were scored only in flies with positive midgut infection. Density scoring (parasites per field): '4' > 1000,
418 '3' 100-1000, '2' 10-100, '1' 1-10, '0' no parasites.
419 **c**, Infection rates and **d**, parasite densities in midgut (MG), proventriculus (PV or cardia) or salivary
420 glands (SG) of tsetse flies infected with *T. brucei* AnTat 1.1E 'Paris' (parent), *flam8* KO (three
421 subclones, KO1, KO2 and KO3) or *in situ* *FLAM8* rescue cells (Institut Pasteur Paris tsetse fly colony).
422 All cell lines express a red fluorescent triple marker⁴⁷. Flies were dissected 28 days p.i.; n (replicates) =
423 2-6, n (flies) = 122 (WT), 88 (KO1), 109 (KO2), 58 (KO3), 40 (resc). Density scoring as in (b).
424 **e**, Developmental progression upon RBP6 overexpression of *carp3* KO trypanosomes compared to the
425 parental RBP6 cell line. Procyclic, epimastigote and metacyclic forms were classified based on stage-
426 specific characteristics including cell size and shape, position of the kinetoplast relative to the nucleus
427 (visualized by staining with DAPI) and expression of stage-specific marker proteins (see Extended Data
428 Fig. 6). >100 cells were analyzed at each time point and replicate. Mean ± SD of n = 3.
429 **f**, Quantification of trypanosomes in different developmental stages (procyclic, long mesocyclic
430 trypomastigote, epimastigote) in posterior midgut (PM) or anterior midgut/proventriculus (AM/PV) of
431 tsetse flies infected with *T. brucei* AnTat 1.1E 'Paris' (parent), *flam8* KO (three subclones KO1, KO2,
432 KO3) or *FLAM8* rescue cell lines. Flies were dissected 28 days p.i. More than 50 trypanosomes were
433 analyzed per fly (2-4 flies per group).

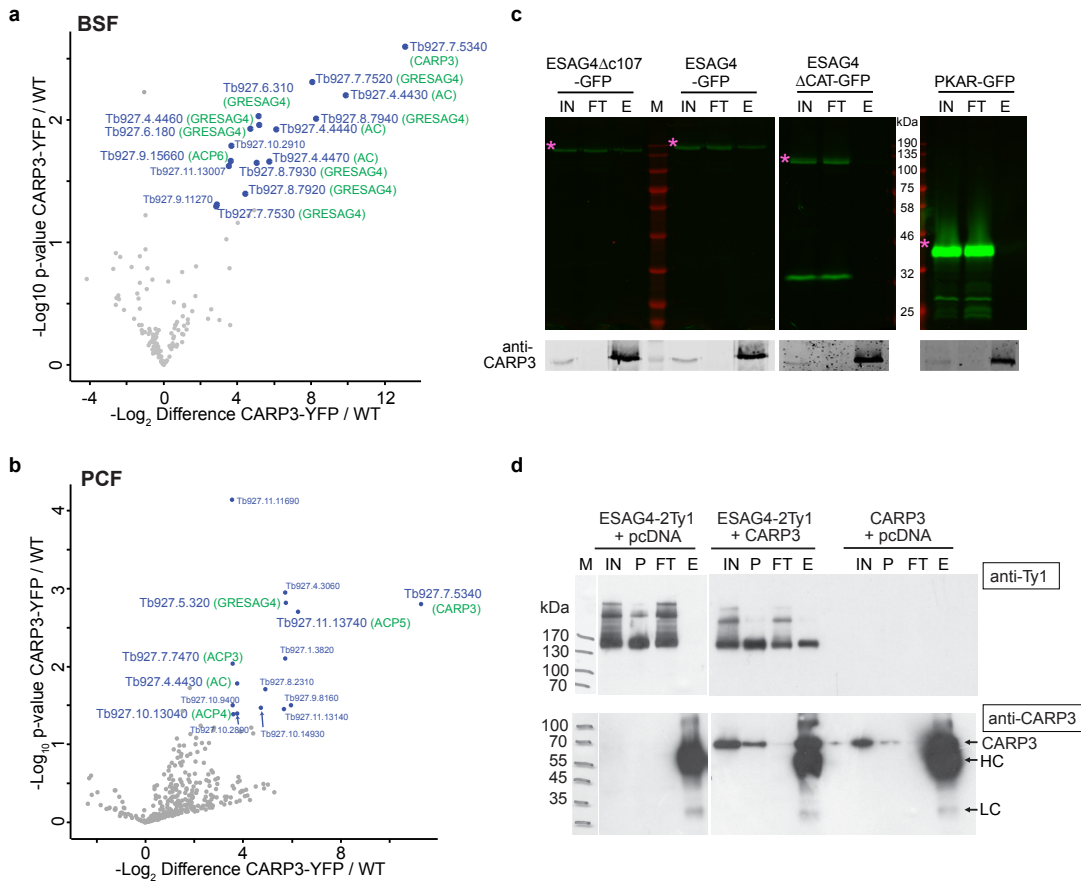
434

435 **CARP3 interacts with ACs**

436 As CARP3 was originally identified as a protein conferring cAMP resistance
437 and is also linked to cAMP via the SoMo phenotype, we tested direct binding
438 of cAMP or association with a cAMP-binding partner. Cyclic AMP coupled to
439 agarose beads pulled down the cAMP-specific phosphodiesterase PDEB1-
440 mNG (positive control) but not CARP3 from procyclic form lysates, indicating
441 that CARP3 is not likely a cAMP-binding protein (Supplementary Fig. 1a). Its
442 expression or localization in PCFs was also unaffected by even extreme
443 intracellular cAMP concentrations elicited by the PDE inhibitors CpdA or
444 CpdB²⁷ (Supplementary Fig. 1b). Such conditions completely inhibited SoMo
445 (Supplementary Fig. 1c), as reported before⁸.
446 Potential CARP3 interaction partners were then identified by GFP-trap pull-
447 downs from *T. brucei* AnTat 1.1E CARP3-YFP of both BSF and PCF (Fig.

448 5a,b and Extended Data Fig. 7a,b). Mass spectrometry analysis identified
449 CARP3 and 11 AC protein groups among the 14 protein groups significantly
450 enriched ($p \leq 0.05$, ≥ 10 -fold enrichment) in BSFs (Fig. 5a, Supplementary
451 Table 2a). In PCFs, CARP3 and 5 AC protein groups were among the 15
452 protein groups showing significant enrichment (Fig. 5b, Supplementary Table
453 2b). For independent confirmation, we selected ESAG4, an abundant, BSF-
454 specific AC, for which an antibody was available³¹. ESAG4 was pulled down
455 by CARP3-YFP (Extended Data Fig. 7c) as well as by native CARP3 (Fig. 5c).
456 For anti-CARP3-mediated pull-down, full-length ESAG4 was expressed as
457 GFP fusion protein (cell line DNi-3 from Salmon et al.³¹) enabling its detection
458 by in-gel fluorescence⁴⁹. To identify the protein domain(s) of ESAG4 required
459 for interaction with CARP3, the intracellular C-terminal tail (107 amino acids,
460 ESAG4Δc107-GFP) following the AC catalytic domain of ESAG4 was
461 truncated (cell line DNi-2³¹). This did not affect CARP3 interaction (Fig. 5c). In
462 contrast, deletion of the AC catalytic domain (cell line ESAG4ΔCAT-GFP)
463 abolished interaction. Both mutant proteins were expressed at a level
464 comparable to full-length ESAG4-GFP (Fig. 5c, input). Mass spectrometry
465 analysis of the reciprocal pull-down from ESAG4-GFP cells provided further
466 confirmation of ESAG4-CARP3 interaction (Extended Data Fig. 7d;
467 Supplementary Table 3). Besides CARP3, other AC isoforms were enriched
468 by ESAG4-GFP pull-down, indicating AC dimerization, as previously
469 reported^{18,26,31}. Consistently, a highly confident homo-dimeric structure was
470 predicted using AlphaFold (Extended Data Fig. 8d). The physical interaction
471 between CARP3 and ACs was independently suggested by a CARP3

472 proximity proteomics approach in BSFs (CARP3 Bioid; details see methods)
473 that revealed a significant enrichment (3-115-fold, FDR ≤ 0.05, $s_0 = 2$) of
474 several AC isoforms (Extended Data Fig. 7e; Supplementary Table 4). In this
475 proximity screen, we also found FLAM8 and calpain 1.3 enriched 125- and
476 83-fold, respectively; a result consistent with the high degree of colocalization
477 of FLAM8, calpain 1.3 and CARP3 in PCFs. Thus, a core complex seems to
478 be maintained at least throughout parts of the parasite life cycle. Physical
479 interaction of CARP3 with PCF-specific flagellar tip-localized AC isoforms was
480 directly shown by pull-down of ACP4-mNG and ACP5-mNG via CARP3
481 (Extended Data Fig. 7f,g). The CARP3-AC interaction was furthermore
482 supported by structural modeling using AlphaFold³⁷ as well as the recently
483 released AlphaFold multimer⁵⁰, which predicted models of CARP3 in complex
484 with each of seven different AC isoforms (ESAG4, GRESAG4.1, ACP1, 3, 4,
485 5, 6). Superposition of all complex models shows a high degree of overall
486 structural similarity (root-mean-square-deviation of 0.8-1.4Å for >90% of all
487 main-chain atoms) (Extended Data Fig. 8a-c). The interface consists of the
488 AC catalytic core and two N-terminal helices (residues 13-41) of CARP3, in
489 perfect agreement with our mutational analysis of the proteins. The interface
490 region has a very high degree of model confidence with a predicted local-
491 distance difference test (pLDDT) score>90 and a low predicted alignment
492 error (PAE) (<5Å). As negative control, structure prediction using AlphaFold
493 for a receptor-type AC of the distantly related kinetoplastid *Bodo saltans* and
494 *T. brucei* CARP3 resulted in a low confidence model with PAE>20Å for
495 putative interface residues.



496

497 **Fig. 5 CARP3 interacts with ACs.**

498 **a, b**, Volcano plot representation of proteins identified upon GFP trap pull-down in *T. brucei* AnTat 1.1E
499 CARP3-YFP cells compared to wild type (WT) in BSFs (**a**) or PCFs (**b**) (n = 2 replicate pull-downs
500 each). Identified proteins are plotted according to p-value and fold change with significantly enriched
501 proteins (p-value ≤ 0.05 , fold change ≥ 10) shown in blue with their TriTrypDB entries. The bait protein
502 CARP3 and AC isoforms are indicated in green.

503 **c**, CARP3 immunoprecipitation (anti-CARP3 coupled to protein A beads) in BSF cell lines expressing
504 ESAG4-GFP, ESAG4ΔC107-GFP, or ESAG4ΔCAT-GFP, respectively. Pull-down assays in a PKAR-
505 GFP cell line served as negative control. Upper panels show detection of GFP by in-gel fluorescence,
506 lower panels show Western blot detection of CARP3. The asterisk labels the fluorescent band
507 corresponding to the respective GFP fusion protein. IN input; FT flow-through; E elution (10x load of
508 input or flow-through); M protein molecular weight marker. HC anti-CARP3 heavy chain

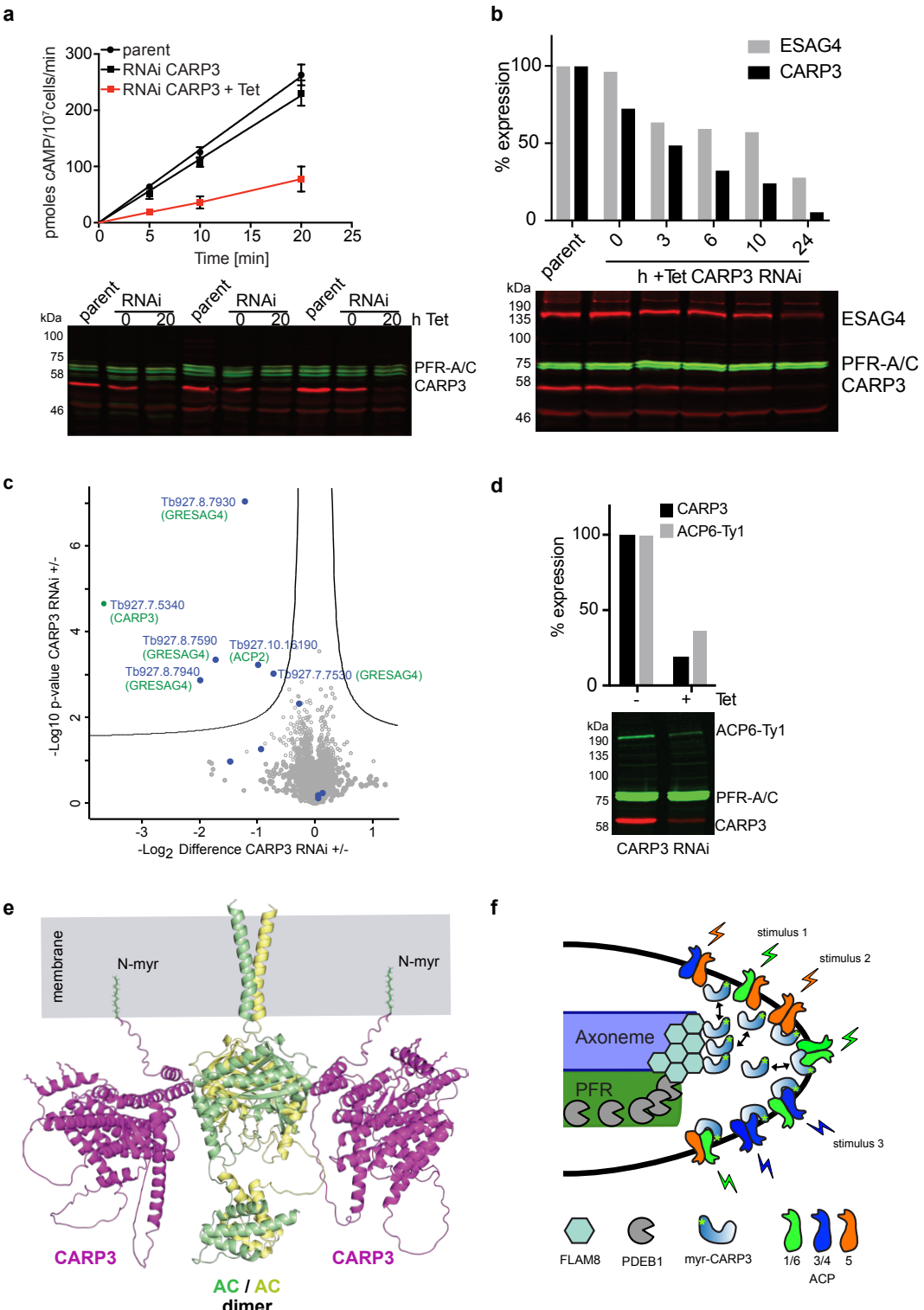
509 **d**, CARP3 immunoprecipitation (anti-CARP3 coupled to protein A beads) from soluble fractions of
510 HEK293 cells expressing CARP3 or ESAG4-2Ty1 or both. Equal amounts of total DNA were transfected
511 in all conditions (ratio of transfected plasmids 1:1). The upper Western blot was probed with anti-Ty1,
512 the lower with anti-CARP3. IN soluble input; P insoluble pellet; FT flow-through; E elution; M protein
513 molecular weight marker; HC anti-CARP3 heavy chain; LC anti-CARP3 light chain.

514

515

516 **CARP3 regulates AC abundance in trypanosomes**

517 We expected the CARP3-AC interaction to modulate AC catalytic activity in
518 the complex. CARP3 and ESAG4 were co-expressed in mammalian HEK293
519 cAMP reporter cells that express luciferase under control of a cAMP response
520 element (CRE). The CARP3-AC interaction was maintained in the
521 heterologous system as shown by pull-down (Fig. 5d). This provided
522 additional evidence for direct physical interaction independent of the parasite
523 cellular environment. Surprisingly, the amount of cAMP produced by
524 recombinantly expressed ESAG4 and normalized to the ESAG4 level was
525 independent of the amount of co-expressed CARP3 in the heterologous HEK
526 cell system (Extended Data Fig. 7h). In contrast, *CARP3* knock down resulted
527 in strongly reduced cAMP production (swell dialysis AC assay) (Fig. 6a) and a
528 decrease in ESAG4 levels over 24 h in BSFs (Fig. 6b). Quantitative
529 proteomics confirmed a 13-fold and ~2-4-fold decrease of CARP3 and five AC
530 groups, respectively (Fig. 6c, Supplementary Table 5). No other significant
531 proteome changes were detected ($p \leq 0.05$). The proteomic data show that
532 CARP3 is a multi-AC regulator (Supplementary Tables 5 and 6). An
533 approximate 3-fold decrease in the expression of ACP6 upon *CARP3* knock
534 down determined by Western blotting in procyclic cells (Fig. 6d) confirmed the
535 regulation in PCF and suggested that the SoMo and fly colonization
536 phenotypes elicited by CARP3 are likely due to changes in AC abundance.
537 Taken together, these results show that CARP3 is a novel modulator of
538 flagellar tip cAMP levels by stabilizing AC abundance in this cAMP
539 microdomain.



540

541 **Fig. 6 CARP3 regulates AC abundance in BSFs and PCFs.**

542 **a**, Total AC activity measured by swell dialysis assay in *T. brucei* MiTat 1.2 13-90 bloodstream forms
543 over 20 min upon Tet-inducible RNAi against *CARP3* ($\pm 1 \mu\text{g/mL}$ Tet for 20 h) with parental 13-90 as
544 control. Mean \pm SD of $n = 9$ (3 independent replicates with 3 measurements each). *CARP3* expression
545 levels were controlled by Western blot with PFR-A/C as loading control ($n = 3$ replicates shown).

546 **b**, Western blot analysis of CARP3 and ESAG4 in *T. brucei* MiTat 1.2 13-90 bloodstream forms upon
547 Tet-inducible RNAi against *CARP3* over 24 h. CARP3 (anti-CARP3) and ESAG4 (anti-ESAG4) signals
548 were normalized to the PFR-A/C loading control and protein expression in the parental cell line was set
549 to 100%.

550 **c**, Volcano plot representation of proteins identified by label-free proteomics in *T. brucei* MiTat 1.2 13-90
551 bloodstream forms upon Tet-inducible RNAi against *CARP3* for 24 h (+) compared to non-induced (-).
552 Proteins are plotted according to p-value and fold change. Protein IDs that differ significantly (p-value ≤
553 0.05, $s_0 = 0.1$) in abundance are located above the significance line. AC isoforms are labeled as blue
554 dots. TriTrypDB entries are indicated for proteins with significantly altered abundance with CARP3 and
555 AC isoforms additionally labeled in green.

556 **d**, Western blot analysis of CARP3 and ACP6-Ty1 in procyclic forms of *T. brucei* 29-13 upon Tet-
557 inducible RNAi against *CARP3* for 24 hours (+Tet) compared to non-induced (-Tet). ACP6 was fused to
558 a C-terminal Ty1 tag in this cell line. CARP3 (anti-CARP3) and ACP6-Ty1 (anti-Ty1) signals were
559 normalized to the PRF-A/C loading control and protein expression in the uninduced condition was set to
560 100%.

561 **e**, Cartoon representation of a model of the CARP3-AC complex at the membrane including the
562 transmembrane helix and the intracellular parts of an AC dimer (ESAG4). CARP3 N-myristylation (N-
563 myr) is indicated. The side chains of several basic amino acids of a membrane-proximal helix predicted
564 for CARP3 are shown. A second CARP3 molecule is shown here, as the AC dimer model sterically
565 allows interaction with two CARP3 molecules.

566 **f**, Model illustrating the relative localization of CARP3, AC, FLAM8 and PDEB1 at the anterior tip of the
567 procyclic trypanosome flagellum. AC homo- and heterodimerization is indicated by different colors with
568 flagellar tip ACs grouped and colored according to their role in SoMo: ACP1/6 (green) inhibit SoMo,
569 ACP5 (orange) promotes SoMo and ACP3/4 (blue) were not linked to SoMo.

570

571

572 **Discussion**

573 In this work, we uncover a novel architecture of a cAMP signaling complex
574 essential for successful arthropod host-parasite interaction and hence
575 transmission of trypanosomes. CARP3, a protein with no sequence
576 homologue outside the genus *Trypanosoma*, interacts with and regulates
577 members of the receptor-type AC family. The model of the complex at the
578 flagellar tip membrane as illustrated in Fig. 6e, is based on orthogonal
579 evidence from reciprocal pull down, BiID proximity labeling, super-resolution

580 microscopy and AlphaFold structure predictions. Phenotypes upon expression
581 of deletion mutants of CARP3 and the ESAG4 cyclase are in full agreement
582 with the high confidence prediction of an interface between the conserved AC
583 catalytic core domain and two N-terminal helices of CARP3. The overlay of
584 independent structure predictions of seven different AC isoforms in complex
585 with CARP3 shows remarkable similarity (Extended Data Fig. 8a,b), further
586 validating the structure prediction and suggesting that CARP3 is a pan-
587 cyclase interactor in trypanosomes. This is in agreement with identification of
588 multiple AC protein groups in CARP3-YFP pull-downs. The N-terminal
589 myristylation of CARP3, revealed by the CARP3Δ3 mutant and previous
590 chemical proteomics data⁴⁵, is essential for tip localization and may enhance
591 AC complex formation by transient membrane interaction of CARP3. N-
592 myristylation confers transient membrane association to proteins, but
593 membrane localization generally needs to be stabilized by a second
594 mechanism, either an interaction with a membrane protein, subsequent
595 palmitoylation or by ionic interactions of basic surface residues with the
596 membrane^{51,52}. CARP3 has not been identified in a palmitoyl proteome⁵³. The
597 structure model allows membrane contact of CARP3 by a helix rich in basic
598 residues and membrane insertion of a myristoyl group attached to CARP3
599 while in complex with ACs (Fig. 6e). Thus, a cooperative effect of AC-
600 interaction, N-myristylation and possibly basic surface residues is likely. A
601 possible mechanism to confine the complex to the tip membrane may be
602 association with lipid rafts that are highly enriched at the procyclic flagellar tip
603 membrane⁵⁴. A lipid raft proteome of PCFs includes CARP3⁵⁵. In mammalian

604 cells, association of ACs with lipid rafts has been described to be isoform-
605 specific. Whereas some mammalian AC isoforms are attracted to lipid rafts,
606 others are enriched outside raft microdomains⁵⁶. A similar mechanism may
607 account for the observed differences in the subflagellar localization pattern of
608 different trypanosome AC isoforms¹⁸. It is conceivable that calpain 1.3 is also
609 part of the same membrane microdomain. Although we have no evidence for
610 a direct physical interaction with the AC-CARP3 complex, PALM microscopy
611 shows extensive colocalization of calpain 1.3 with CARP3 at single molecule
612 resolution at the procyclic flagellar tip, and BioID with CARP3 as bait identifies
613 calpain 1.3 (83-fold enriched) in BSF. As calpains are linked to Ca²⁺ signaling
614 in other systems, calpain 1.3 may be involved in Ca²⁺-regulation of
615 trypanosome ACs, a property that has been reported earlier for some
616 trypanosome ACs⁵⁷⁻⁶⁰. Calpain 1.3 differs from classical calpains by lacking
617 some of the features critical for catalytic Ca²⁺-dependent protease activity¹⁴.
618 CARP3 may serve a scaffolding role for recruitment of additional proteins in
619 AC signaling complexes. Significant hits in the BioID interaction screen and
620 the presence of intrinsically disordered regions (IDR loops) on the cytoplasmic
621 face of the CARP3 structure model (Fig. 6e) are compatible with this
622 interpretation. IDRs often provide a platform for multiple weak interactions in
623 signaling complexes and are more likely to phase separate. An example is the
624 membrane associated pLAT-Grb2-Sos1 condensate in T-cell receptor
625 activation⁶¹. A fraction of CARP3 at the flagellar tip does not localize at the
626 membrane but colocalizes with the cytoskeletal scaffold protein FLAM8,
627 previously positioned at the plus end of the axonemal microtubules in PCF¹⁵

628 and also distributed along the flagellum in BSF⁶². The close proximity and
629 likely interaction of CARP3 and FLAM8 is supported by BiOID in BSF (125-fold
630 enrichment of FLAM8 with two biotinylation sites identified). Flagellar tip
631 localization of CARP3 is dependent on FLAM8; in its absence, CARP3 still
632 entered the flagellum but was not enriched at the tip. In the short epimastigote
633 stage, CARP3 also followed the FLAM8 redistribution along the length of the
634 flagellum⁶². FLAM8 therefore seems to provide a reservoir for CARP3 at the
635 flagellar tip in PCF, possibly to increase its local concentration. This may
636 indicate dynamic properties of the AC-CARP3 complex. The intraflagellar
637 transport (IFT) machinery is required for flagellar tip localization of FLAM8⁶³,
638 and possibly also of CARP3. The complex of CARP3 with AC isoforms was
639 detected in both stages (BSFs and PCFs). The proximity of CARP3 to FLAM8
640 and calpain 1.3, supported by super-resolution microscopy in PCF and by
641 BiOID in BSF, suggests that similar complexes are present in several stages
642 of the parasite's life cycle. So far, only phenotypes dependent on localization
643 at the procyclic flagellar tip have been observed. In contrast to the
644 aforementioned interactions, PDEB1 is not enriched in the tip microdomain
645 but forms a gradient with a higher concentration close to the flagellar tip and a
646 lower concentration at the flagellar base (Extended Data Fig. 2b). This
647 indicates a diffusion barrier function to establish a cAMP microdomain at the
648 tip in analogy to comprehensive studies in the mammalian system²³.

649 CARP3 deletion completely blocks trypanosome SoMo, and
650 interestingly, the absence of CARP3 from the flagellar tip (in $\Delta flam8$ and
651 $carp3\Delta 3$) is alone sufficient for this phenotype. Genetic or pharmacological

652 inhibition of PDEB1 was reported to abolish SoMo⁸ and a similar phenotype
653 seems to result from a single allele knock out (sKO) of the flagellar tip cyclase
654 ACP5 according to a recent preprint⁶⁴. Therefore, genetic evidence indicates
655 that these proteins work together in a cAMP signaling pathway required for
656 SoMo. This pathway has been suggested to also control the parasite's ability
657 to orient and successfully migrate in the insect digestive tract to ultimately
658 reach the salivary glands and complete the infectious cycle^{9,65}. In agreement
659 with this hypothesis, $\Delta carp3$ and $\Delta flam8$ mutants are unable to colonize the
660 salivary glands upon tsetse infections. We are aware of the complication that
661 colonization phenotypes can equally result from impact on the various
662 developmental transitions and adaptations along the parasite's journey in the
663 fly. Importantly, in contrast to previous studies, we provide a high degree of
664 phenotypic specificity: (1) Both $\Delta carp3$ and $\Delta flam8$ cell lines do not show any
665 growth or flagellar motility phenotypes in culture. (2) $\Delta carp3$ can proceed
666 through complete differentiation in the RBP6-induced culture model with wild
667 type level of metacyclogenesis, thus excluding a cell autonomous defect of
668 the developmental program. Furthermore, the $\Delta flam8$ cell line that delocalizes
669 CARP3 developed into epimastigote stages *in vivo* in the tsetse alimentary
670 tract. (3) Relocalization of CARP3 away from the tip by either deletion of
671 *FLAM8* or by deletion of the myristoylation site in *CARP3* is equally sufficient
672 to abolish SoMo. (4) For all phenotypic analyses, clones of the fly
673 transmissible pleomorphic AnTat 1.1 strain and freshly differentiated procyclic
674 forms of this strain were used. Fly transmissions were done in two different
675 laboratories with several independent KO lines and rescue lines. (5) Fly

676 infection phenotypes are very similar for $\Delta carp3$ and $\Delta flam8$, although the
677 absolute infection rate differs between the AnTat 1.1 clones and fly colonies in
678 the two laboratories. Not a single trypanosome reached the salivary glands,
679 even in flies with positive cardia infection, yet both mutants were able to
680 colonize the cardia with reduced rate and at lower densities compared to WT.
681 In contrast, the $\Delta pdeb1$ mutant⁹ was not able to colonize the ectoperitropic
682 space and could not establish a cardia infection. The different phenotype may
683 indicate involvement of PDEB1 in additional steps of development or in
684 parasite fitness in the tsetse fly or be due to the inherent fly transmission
685 defect of the laboratory-adapted monomorphic Lister 427 strain⁶⁶⁻⁶⁸ used by
686 Shaw, et al. ⁹. Interestingly, in long trypomastigotes and long dividing
687 epimastigotes colonizing the anterior midgut, cardia and foregut, i.e. in the
688 migrating stages, FLAM8 is progressively enriched at the flagellar tip
689 microdomain (Fig. 3i; ⁶²), where CARP3-AC complexes are required. FLAM8
690 and consequently CARP3 are redistributed from the tip to the length of the
691 flagellum in short epimastigotes, a life cycle stage that normally attaches to
692 the salivary gland epithelium via the flagellar membrane⁶⁹. The change in
693 subcellular localization may be cause or consequence of this attachment, but
694 the salivary gland colonization defect suggests a role of the tip signaling
695 complex prior to attachment. Together, $\Delta carp3$ and $\Delta flam8$ phenotypes
696 provide the best available evidence that an AC signaling complex controls a
697 crucial process leading to the colonization of fly salivary glands and thus
698 parasite transmission. In this context, the SoMo phenotype *in vitro* serves as
699 proxy for this complex process *in vivo*, rendering the signaling mechanisms

700 experimentally more amenable. This is independent of the question whether
701 trypanosomes display true swarming, defined as directional motility of groups
702 of cells, mainly observed in prokaryotic systems⁶. A careful analysis of the
703 SoMo process on plates showed that single fluorescently labeled
704 trypanosomes in projections did not move directionally and single cell motility
705 did not correlate with movement of the projections⁷⁰. In dissected tsetse fly
706 tissues, collective motion of trypanosomes as synchronized swarms with
707 coordinated flagellar beat were observed *ex vivo*¹¹. Chemotaxis seems to be
708 an obvious link between the projections *in vitro* and the directional migration in
709 the tsetse alimentary tract. Chemotaxis has recently been described for
710 trypanosomes *in vitro*⁷¹. Metabolites derived from tsetse fly tissues or
711 endosymbionts of the tsetse and tissue surfaces have been suggested as
712 possible cues. A recent preprint demonstrated pH taxis of trypanosomes
713 undergoing SoMo on agarose plates⁶⁴. Indeed, the trypanosomal receptor-
714 type ACs have been hypothesized to be activated by binding of ligands to
715 their extracellular part containing two VFT (Venus fly trap) domains^{26,72}
716 homologous to ligand-binding surface proteins in other systems⁷³. However,
717 the membrane stress-induced activation of ACs by low osmolarity or low
718 pH^{26,74-76} has not been linked to a specific domain or ligand binding event so
719 far. Membrane stress may also result from parasite attachment to insect host
720 tissue surfaces or cell-cell contacts in highly confined space, as observed for
721 swarming *P. aeruginosa*⁷⁷. As some trypanosome ACs seem to be activated
722 by calcium *in vivo*⁵⁷⁻⁶⁰, the report of a membrane tension-mediated opening of

723 a mechanosensitive ion channel in *T. cruzi*⁷⁸ may merit follow-up in this
724 context.

725 Although the precise role of CARP3 in AC regulation remains to be
726 established, stabilization of several AC isoforms was obvious from rapid
727 decrease of AC abundance upon RNAi-mediated depletion of CARP3. Thus,
728 a role of the complex in AC receptor recycling or desensitization is a
729 reasonable hypothesis. Most AC interacting proteins reported so far in other
730 systems are regulators of AC activity such as mammalian snapin⁷⁹ or yeast
731 CAP1⁸⁰. However, Hu, et al.⁸¹ reported a novel AC-interacting protein called
732 TRIP-Br1 (transcriptional regulator interacting with the PHD bromodomain 1)
733 that regulates AC turnover by physically connecting multiple AC isoforms to
734 the E3 ubiquitin ligase XIAP in mammalian cells. In turn, XIAP ubiquitinates a
735 conserved lysine residue in AC isoforms thereby accelerating endocytosis and
736 degradation. Previous studies have shown that the turnover of
737 transmembrane surface proteins in trypanosomes can be regulated by
738 ubiquitylation^{82,83}, but the parasite's ACs were not among the proteins
739 downregulated upon individual depletion of two deubiquitylating enzymes.

740 Given the SoMo phenotypes observed in mutants of CARP3, of several tip
741 localized ACs, and of PDEB1, and the well-supported assumption that these
742 proteins all impact on SoMo via changes in cAMP concentration at the
743 flagellar tip [$cAMP^{tip}$] or in the cAMP gradient along the flagellum, the
744 challenge is to integrate this information into a consistent model. It appears
745 contradictory that the $\Delta carp3$ line and the sKO of *ACP5*⁶⁴, both expected to
746 reduce [$cAMP^{tip}$], abolish SoMo, while RNAi-mediated depletion of ACP1 or

747 ACP6 (also expected to reduce [cAMP^{tip}]) has apparently the opposite effect⁷.
748 The SoMo-negative phenotype of *Δpdeb1* (expected increase of [cAMP])⁹ is
749 here interpreted as mechanistically distinct, as PDEB1 is not tip localized and
750 the mutant likely disrupts global [cAMP] and flagellar cAMP gradients. Based
751 on the predicted AC dimerization (Fig. 6e, Extended Data Fig. 8d)^{57,84} that has
752 also been shown *in vivo*^{18,29,31}, we propose a new model for AC regulation
753 (Fig. 6f). Dominant-negative heterodimer formation has previously been
754 described for invertebrate soluble guanylate cyclase (GC)⁸⁵, mammalian AC8
755 in vascular smooth muscle cells⁸⁶ and also ESAG4 of trypanosomes³¹.
756 Different trypanosome AC isoforms may have different intrinsic cyclase
757 activities and may be activated or inhibited by different stimuli. Upon
758 heterodimerization, this may result in activation or dominant-negative
759 inhibition, dependent on AC isoform composition of the tip domain and
760 changing environmental stimuli to fine-tune cAMP levels. In agreement to the
761 model, AC isoform diversity and non-redundancy at the flagellar tip⁷ and
762 differential expression of transcripts encoding AC isoforms in trypanosomes
763 colonizing midgut, cardia or salivary glands^{34,35} have been reported. CARP3
764 depletion might result in local compositional imbalance of AC isoforms
765 possibly due to isoform-specific quantitative differences in CARP3-mediated
766 complex stability. It is conceivable that AC complex signaling is required at
767 several locations and bottlenecks in the fly alimentary tract and that different
768 AC isoforms respond to different environmental cues. Our model implies that
769 future research should first focus on the AC family to unravel the cAMP
770 signaling initiated at the flagellar tip. Detailed biochemical and structural
771 analyses are required to identify AC-activating ligands and better understand

772 the mechanism of cyclase activation, the role of homo- and heterodimerization
773 and the unique isoform diversity and stage regulation of the trypanosomal AC
774 family. Using the SoMo phenotype as simple *in vitro* assay, a key signaling
775 system coordinating host-parasite communication and securing successful
776 transmission of the parasite becomes accessible.

777

778

779 **Methods**

780 **Trypanosome culture conditions**

781 Bloodstream forms of the pleomorphic *Trypanosoma brucei brucei* strains
782 AnTat 1.1 'Munich' or AnTat 1.1E 'Paris'³⁹ were cultivated at 37°C and 5%
783 CO₂ in modified HMI-9 medium⁸⁷ supplemented with 10% (v/v) heat-
784 inactivated fetal bovine serum (FBS) and 1.1% methylcellulose (only for AnTat
785 1.1 'Munich'). Cell density was monitored using a haemocytometer and was
786 kept below 8 × 10⁵ cells/mL for continuous growth of replicative long slender
787 bloodstream forms. Procyclic stage cells were generated by density-
788 dependent differentiation of long slender bloodstream forms to growth-
789 arrested short stumpy bloodstream forms (culture with starting density of 5 ×
790 10⁵ cells/mL was grown for 36 hours without dilution). Short stumpy forms
791 were transferred into modified DTM medium⁸⁸ complemented with 15% (v/v)
792 heat-inactivated FBS at 2 × 10⁶/mL, followed by addition of 6 mM cis-
793 aconitate and cultivation at 27°C. Procyclic forms of AnTat 1.1 'Munich', AnTat
794 1.1E 'Paris', AnTat 1.1 EATRO1125 T7T or MiTat 1.2 29-13⁸⁹ were grown at

795 27°C in SDM-79 medium⁹⁰ supplemented with 10% (v/v) heat-inactivated FBS
796 and 20 mM glycerol.

797

798 **In vitro differentiation by RBP6 overexpression**

799 Differentiation of procyclic forms by overexpression of RBP6 was performed
800 in EATRO 1125 T7T as described previously^{48,91}.

801

802 **Cloning and generation of transgenic trypanosomes**

803 Generation of a homozygous carp3 knock out:

804 Both *CARP3* alleles were deleted from AnTat 1.1 bloodstream forms or
805 EATRO1125 procyclic forms carrying the RBP6 overexpression construct by
806 transfection with pTBT-based plasmids⁹² containing *CARP3* 5'UTR and
807 3'UTR sequences flanking a hygromycin or blasticidin resistance cassette
808 (kindly provided by Daniel Tagoe and Harry de Koning, Glasgow). Plasmids
809 were digested with NotI and Xhol for transfection according to standard
810 electroporation conditions⁹³ and cells were selected with 2 µg/mL hygromycin
811 B or 2 µg/mL blasticidin, respectively.

812 Generation of endogenous CARP3 rescue and CARP3Δ3 rescue cell lines:

813 An endogenous *CARP3* rescue cell line was generated by transfection of the
814 hemizygous *carp3* KO cells resistant to hygromycin with a pEnT6B-based
815 plasmid⁹⁴ that contained the *CARP3* 5'UTR amplified with primers MG30 and
816 MG31 from genomic DNA as well as the first 300 nucleotides of the *CARP3*
817 ORF amplified with primers MG32 and MG33. The plasmid was linearized
818 with NotI for transfection and cells were selected with 2 µg/mL blasticidin. The

819 same strategy was used for replacement of endogenous CARP3 by
820 CARP3 Δ 3 using forward primer CARP3 Δ 3_HindIII_fw instead of MG30 for
821 amplification of the CARP3 ORF N-terminus with deletion of nucleotides 4-12.

822 Generation of a homozygous *flam8* knock outs and rescue:

823 In AnTat 1.1E ‘Paris’ bloodstream forms, one *flam8* allele was deleted and the
824 second one truncated to generate *flam8* knock-outs sub-clones as described
825 in⁴⁶. A rescue sequence was then re-introduced in the partially deleted allele
826 to produce an add-back strain⁴⁶.

827 Tetracycline-inducible RNAi of CARP3:

828 Two copies of a tetracycline repressor were integrated into the *T. brucei*
829 AnTat 1.1 ‘Munich’ genome by transfection with the NotI-linearized plasmid
830 pHD1313⁹⁵. Antibiotic selection was performed with 10 μ g/mL phleomycin.
831 This cell line was further transfected with pHD615[PAC]CARP3_RNAi, a
832 plasmid allowing hairpin RNAi-mediated repression of CARP3. Two fragments
833 of the CARP3 ORF (nt 514 to 913; nt 514 to 965) were PCR-amplified from
834 AnTat 1.1 genomic DNA using primers CARP3_hairpin_up_HindIII and
835 CARP3_hairpin_sense_Xhol or CARP3_hairpin_up_BamHI and
836 CARP3_hairpin_antisense_Xhol, respectively, and cloned into pHD615[PAC]
837 by a three-component-ligation. Cells transfected with the Ncol-linearized
838 plasmid were selected with 0.1 μ g/mL puromycin.

839 For generation of a tetracycline-inducible CARP3 RNAi cell line in procyclic
840 Lister 427 29-13, the plasmid p2t7-177[BLE]-CARP3 (Gould et al 2013) was
841 used for transfection and selection was carried out with 2.5 μ g/mL
842 phleomycin.

843 *C-terminal in situ tagging of CARP3 with YFP or mNeonGreen:*
844 The *CARP3* C-terminus was amplified from genomic DNA (strain AnTat 1.1)
845 using primers p3074_CARP3_up_Swal and p3074_CARP3_low_BamHI and
846 cloned into the vector p3074⁹⁴ that enables C-terminal Ty1-tagging. The 4x
847 Ty1-tag was swapped to YFP from p3329 using BamHI and EcoRI. For PALM
848 microscopy, YFP from p3329 was replaced by mNeonGreen amplified from
849 plasmid pK19msB-mNeonGreen-ptsG⁹⁶ by primers mNeon_BamHI_fw and
850 mNeon_EcoRI_rev. The plasmids were linearized with NotI and transfected
851 cells were grown in the presence of 2 µg/mL G418 or 0.1 µg/mL puromycin.
852 *C-terminal in situ tagging of CARP3 with mCherry or photoactivatable*
853 *(PA)mCherry:*
854 For C-terminal fusion of CARP3 to mCherry, the long primer PCR tagging
855 strategy was used⁹⁷. YFP-Ty1 of plasmid pPOTv4 was replaced by mCherry-
856 Ty1 followed by PCR amplification of mCherry-TY with primers
857 pPOTv4_Lr_mCherry_TY_CARP3 fw and pPOTv4_Lr_mCherry_TY_CARP3
858 rev introducing stretches homologous to the C-terminus of the *CARP3* ORF
859 and the start of the *CARP3* 3'UTR. The PCR product was purified by phenol-
860 chloroform extraction prior to transfection and selection was done with 2
861 µg/mL G418. For C-terminal fusion of CARP3 to photoactivatable
862 (PA)mCherry, the same strategy was used. mCherry-Ty1 was replaced by
863 PAmCherry amplified from plasmid pK19mobsacBparB-PAmCherry⁹⁸ using
864 primers PAmCherry BamHI FWD and PAmCherry SacI REV.
865 *Overexpression of C-terminally Ty1-tagged CARP3 or CARP3 truncations.*

866 C-terminal TY-tag fusions of full-length CARP3, CARP3 N-terminus (1-337) or
867 CARP3 C-terminus (171-end) were generated by PCR on genomic DNA of *T.*
868 *brucei* AnTat 1.1 using primers CARP3_fw_HindIII or CARP3_Ct_fw_HindIII
869 and CARP3_Ty1_Ct_rev_BamHI or CARP3_Ty1_Nt_rev_BamHI,
870 respectively, followed by ligation via BamHI/HindIII into the pTSARib
871 overexpression vector⁹⁹ with a puromycin resistance cassette²⁴. Constructs
872 were transfected into AnTat 1.1 CARP3 knockout cells and selected with 0.1
873 µg/mL puromycin.

874 *Inducible expression of CARP3-BirA*-Ty1 for proximity proteomics.*
875 Primers CARP3_fw_HindIII and CARP3_NoSTOP_Spel were used to amplify
876 the CARP3 ORF that was inserted together with a downstream BirA*-Ty1
877 cassette via HindIII, Spel and BamHI restriction sites into plew100v5b1d-BLE,
878 a modified version of the original plew100 vector⁸⁹.

879 *C-terminal in situ tagging of FLAM8 with YFP or mNeonGreen:*
880 For C-terminal in situ tagging of FLAM8 with YFP, *T. brucei* AnTat 1.1 was
881 transfected with p3329.FLAM8¹⁵ followed by selection with 0.1 µg/mL
882 puromycin. For PALM microscopy, YFP was swapped to mNeonGreen using
883 BamHI and EcoRI. The plasmids were linearized with NruI and transfected
884 cells were grown in the presence of 0.1 µg/mL puromycin.

885 *C-terminal in situ tagging of calpain 1.3 with mNeonGreen:*
886 For C-terminal in situ tagging of calpain 1.3 with mNeonGreen, the *calpain 1.3*
887 C-terminus was amplified from genomic DNA using primers
888 p3074_Calp1.3_fw and p3074_Calp1.3_rev and cloned into

889 p3329.mNeonGreen via KpnI and BamHI. The plasmid was linearized with
890 NruI and transfected cells were selected with 0.1 µg/mL puromycin.

891 C-terminal in situ tagging of PDEB1 with mNeonGreen:

892 For C-terminal in situ tagging of PDEB1 with mNeonGreen, the *PDEB1* C-
893 terminus was amplified from genomic DNA using primers PDEB1_KpnI_fw
894 and PDEB1_BamHI_rev and cloned into p3329.mNeonGreen via KpnI and
895 BamHI. The plasmid was partially digested with NdeI and transfected cells
896 were selected with 0.1 µg/mL puromycin.

897 C-terminal in situ tagging of ACP1, ACP3, ACP4, ACP5 or ACP6 with Ty1 or
898 mNeonGreen:

899 C-terminal Ty1 tagging of ACP1 or ACP6, respectively, was performed similar
900 to previously described by Saada et al.¹⁸ using the in situ tagging vector
901 pMO2T¹⁰⁰ and primers ACP1orfF/ACP1orfR and ACP1utrF/ACP1utrR or
902 ACP6orfF/ACP6orfR and ACP6utrF2/ACP6utrR2, respectively. The Ty1 tag
903 was swapped for mNeonGreen in plasmid pMO2T_ACP1 using primers
904 mNeon_Xhol_fw and mNeon_Sall_rev and Xhol/Sall digestion. ACP1 ORF
905 and 3'UTR fragments were replaced by KpnI/Xhol or BamHI/XbaI swap,
906 respectively, with ACP3, ACP4 or ACP5 ORF and 3'UTR fragments using
907 primers ACP3_, ACP4_ or ACP5_ORF_FW/REV and UTR_FW/REV,
908 respectively, resulting in plasmids pMO2mNG_ACP3, pMO2mNG_ACP4 and
909 pMO2mNG_ACP5. The plasmids were digested with EcoRV and NsiI
910 (pMO2mNG_ACP3), KpnI and PstI (pMO2mNG_ACP4) or KpnI and SphI for
911 transfection of procyclic AnTat 1.1 or 427 29-13 cells and selection was
912 carried out with 1 µg/mL puromycin.

913 Tetracycline-inducible overexpression of ESAG4ΔCAT with C-terminal GFP
914 tag
915 The plasmid plew82.ESAG4ΔCAT-2Ty1 (deletion of nucleotides 2680 to 3318
916 of ESAG4 ORF) was generated using the In-Fusion® HD Cloning Kit
917 (Takara), Phusion® High-Fidelity DNA Polymerase (NEB) and primers
918 DCAT_Mut1 and DCAT_Mut2 oriented in opposite directions with 19 bp
919 overlaps on the template vector plew82.ESAG4-2Ty1. The linear plasmid was
920 circularized in an In-Fusion reaction according to the manufacturer's
921 instructions. In order to obtain plew82.ESAG4ΔCAT-GFP, a 733 bp
922 KpnI/BamHI fragment (containing EGFP) from plew82.ESAG3-DNi-2³¹ was
923 inserted into the KpnI/BamHI digested plew82.ESAG4ΔCAT-2Ty1.
924 Linearization was done with NotI and transfected cells were selected with 2.5
925 µg/mL phleomycin.
926 Constitutive overexpression of catalytically inactive ESAG4-GFP.
927 Catalytically inactive ESAG4 with point mutations D948A and R1052A fused
928 to a C-terminal GFP (ESAG4 DNi-3 from³¹) was cloned into the constitutive
929 expression vector pTSARib⁹⁹ via HindIII and BamHI restriction sites. The
930 plasmid was linearized with SphI and transfected into BSFs of *T. brucei* strain
931 MiTat 1.2 13-90 CARP3 RNAi³⁰.
932 Constitutive overexpression of PKAR-GFP.
933 The N-terminus of *T. brucei* PKAR (protein kinase A regulatory subunit;
934 Tb927.11.4610, amino acids 1-200) was fused to C-terminal GFP and cloned
935 into the constitutive expression vector pTSARib⁹⁹ via a 3-component ligation
936 using HindIII and EagI (PKAR fragment) and EagI and BamHI (GFP)

937 restriction sites. Linearization was done with SphI and transfected cells were
938 selected with 2 µg/mL hygromycin B.

939 Plasmids for expression of CARP3 and ESAG4-2Ty1 in HEK 293 cells.

940 The ESAG4 C-terminus (nt 2424 to 3804) was amplified from a plasmid
941 containing the full ESAG4 (BES1/TAR40.13) ORF using primers
942 ESAG4_fwd_BstBI and ESAG4-2Ty1_rev_BamHI introducing a C-terminal
943 2xTy1 tag. The fragment was ligated into plew82.ESAG4-DNi-1³¹ cut with
944 BstBI and BamHI, resulting in plasmid plew82.ESAG4-2Ty1. ESAG4-2Ty1
945 was cut out with BamHI and HindIII and cloned into pcDNA3.1(+).

946 The CARP3 ORF was amplified from plasmid pTSARib.CARP3-Ty1 using
947 primers CARP3_fw_HindIII and CARP3_rev_Apal and cloned into
948 pcDNA3.1(+) via HindIII and Apal.

949 A list of all primers used in this study is provided as Supplementary Table 7.
950 All transfections were done in slender bloodstream forms, except for tagging
951 of ACPs.

952

953 **Dual-luciferase® reporter assay in HEK cAMP reporter cells.**

954 Human embryonic kidney cells 293T (HEK 293T) were cultured in DMEM/F12
955 medium (Lonza) supplemented with 10% heat-inactivated FBS, 100 U/mL
956 penicillin and 100 µg/mL streptomycin in a 5% CO₂ humidified incubator at
957 37°C. 2 × 10⁵ HEK 293T cells were plated into 12-well plates and transfected
958 after 24 h in triplicate with the plasmids pGL4.29[luc2P/CRE/Hygro]
959 (Promega), pRL-SV40 (Renilla Luciferase), pcDNA3.1(+)ESAG4-2Ty and
960 pcDNA3.1(+)CARP3 using Lipofectamine 2000 (Invitrogen) according to the

961 manufacturer's instructions. The amount of plasmid DNA transfected per well
962 was optimized for each expression vector as follows: Renilla luciferase (5 ng),
963 Luc2P (250 ng), ESAG4 (250 ng) and CARP3 (62.5 to 500 ng). For the
964 different conditions, the amount of pcDNA3.1(+)CARP3 varied while keeping
965 a constant concentration of pcDNA3.1(+)ESAG4-2Ty1 (ESAG4:CARP3 ratios:
966 1:0, 1:0.25, 1:0.5, 1:1, 1:2, 0:1). The total amount of DNA in each well was
967 adjusted to 1 μ g with the empty pcDNA3.1(+) vector. 24 hours after
968 transfection, cells were collected, and washed 2x with PBS. 5×10^4 cells were
969 harvested in passive lysis buffer (Promega) and the activities of the Firefly
970 and Renilla luciferases were measured sequentially using the Dual-
971 Luciferase® Reporter Assay System (Promega, cat. no. E1980).
972 Luminescence measurements were performed for 10 s at room temperature
973 by a Centro XS3 LB 960 luminometer (Bertold Technologies, Bad Wildbad,
974 Germany) provided with Mikrowin 2000 v.4.41 software (Mikrotek Labsis
975 Laborsysteme GmbH). The light resulting from cleavage of the two substrates
976 was quantified as relative light units (RLU). Firefly:Renilla ratio was calculated
977 by dividing firefly RLU by the Renilla RLU. The assay was performed in
978 triplicate for each sample.
979 The rest of the cell pellets were resuspended in Laemmli buffer (2.5×10^3
980 cells/ μ L) and used for Western blot analysis.

981

982 **AC assays**

983 AC assays were performed according to Salmon et al.²⁹ after mild acid (pH
984 5.5) treatment. Briefly, cultures of *T. brucei* MiTat 1.2 CARP3 RNAi cells were

985 grown to a density of around 2×10^5 cells/mL, followed by RNAi induction with
986 1 $\mu\text{g}/\text{mL}$ doxycycline for 24 h. The cells were harvested at a density of $\sim 1 \times$
987 10^6 cells/mL by centrifugation, washed twice with ice-cold phosphate-buffered
988 saline/glucose (PSG) buffer (137 mM NaCl, 2.7 mM KCl, 8.1 mM Na₂HPO₄,
989 1.8 mM KH₂PO₄, 1.5% glucose, pH 8.0) and after final counting resuspended
990 in “swell dialysis” buffer of low osmotic strength (50 mM KCl, 5 mM MgCl₂, 1
991 mM glucose, 1 mM EGTA, 1X cOmplete EDTA-free protease inhibitor
992 cocktail, 13.3 mM TES, pH 5.5) at a density of 5×10^8 cells/mL for 1 h at 4 °C.
993 The reaction was started by addition of 20 μL sample (1×10^7 cells) to 80 μL
994 assay cocktail (0.5 mM cAMP, 10 mM phosphocreatine, 50 units/mL creatine
995 kinase, 1 mM EGTA, 10 mM MgCl₂, 20 mM KCl, 0.5 mM ATP, 1 mM glucose,
996 1× cOmplete EDTA-free protease inhibitor cocktail, 25 mM TES pH 5.5 and
997 0.8 μCi of [α -32P]-ATP at 10-40 Ci/mmol) and was incubated for 5, 10 and 20
998 min at 37°C. Each reaction was stopped by adding 100 μL of stop solution
999 (2% SDS, 40 mM ATP, 0.01 M cAMP). [³²P]cAMP was isolated by two-step
1000 chromatography according to Salomon et al.¹⁰¹ and measured by liquid
1001 scintillation counting. Each assay was carried out in triplicate. AC activity was
1002 calculated by linear regression analysis of the rate of cAMP production.

1003

1004 **Cell motility assay**

1005 Procyclic forms of *T. brucei* strain AnTat 1.1 were resuspended in 70%
1006 SDM79, 10% FCS, 0.6% (v/v) methylcellulose at a density of 8×10^6 cells/mL
1007 and placed onto a glass slide. 12 regions of each slide were imaged on a
1008 Leica DMI600B series inverted microscope (Leica Microsystems). Cells were

1009 imaged over a period of 15 seconds, yielding 31 data points for each cell. All
1010 cells which were in view for the entire 15-second measurement period were
1011 included in the analysis. At least 50 cells were included for each cell line
1012 tested. Tracking and subsequent calculation of motion metrics was performed
1013 using the MTrackJ plugin for ImageJ¹⁰². Statistical significance was
1014 determined by one-way ANOVA with $p \leq 0.05$ considered statistically
1015 significant.

1016 For the FLAM8 mutant panel, movies (150 frames, 50 ms exposure) were
1017 recorded in warm SDM79 medium with 1.1% methylcellulose at 1×10^6
1018 cells/mL under the 10x objective of an inverted DMI4000 LEICA microscope
1019 (Leica Microsystems) coupled to a Retiga-SRV camera (QImaging). Movies
1020 were converted with the MPEG Streamclip V.1.9b3 software (Squared 5) and
1021 analyzed with the MedeaLAB CASA Tracking V.5.5 software (Medea AV
1022 GmbH), as described in Rotureau et al.¹⁰³.

1023

1024 **Social motility assay**

1025 Agarose plates for social motility assays were prepared as described⁵. $5 \times$
1026 10^5 cells of *T. brucei* strain AnTat 1.1 or AnTat 1.1E were spotted in $5 \mu\text{L}$ of
1027 SDM-79 on agarose plates within 7 days after density-dependent
1028 differentiation from bloodstream to procyclic stage.

1029

1030 **Generation of polyclonal antibodies**

1031 The *CARP3* ORF was cloned as N-terminal His₁₀ fusion into pETDuet-1 using
1032 primers Tb927.7.5340F10His and Tb927.7.5340_BamHI_rev via Ncol and

1033 BamHI restriction sites and transformed into *E. coli* Rosetta. 500 µg of His₁₀-
1034 CARP3 purified using a Ni-NTA column (Qiagen) were used for immunization
1035 of rabbits by Eurogentec, followed by further boosts with 500 µg antigen. The
1036 CARP3 antiserum was affinity-purified using His₁₀-CARP3 according to the
1037 method of Olmsted¹⁰⁴.

1038

1039 **In-gel fluorescence**

1040 In-gel fluorescence analysis was carried out as described previously⁴⁹. Briefly,
1041 trypanosomes were lysed in 1 × Laemmli sample buffer (125 mM Tris pH 6.8,
1042 4% (w/v) SDS, 20% (v/v) glycerol, 10% 2-mercaptoethanol, 0.02% (w/v)
1043 bromophenol blue) to a density of 3 × 10⁶/µL. Samples were sonicated
1044 (Bioruptor®, Diagenode (Belgium); settings: high energy, 4 cycles, 30 s
1045 on/off) and immediately subjected to 10% SDS PAGE. The gel was scanned
1046 with a Typhoon Trio Variable Mode Imager System (GE Healthcare) at $\lambda_{\text{ex}} =$
1047 488 nm and $\lambda_{\text{em}} =$ 526 nm for mNeonGreen and at $\lambda_{\text{ex}} =$ 670 nm and $\lambda_{\text{em}} =$
1048 633 nm for visualization of the Blue Prestained Protein Standard (NEB).

1049

1050 **Western blot**

1051 Western blot analysis was performed as previously described²⁹. Primary
1052 antibodies used are anti-CARP3 (1:500), anti-ESAG4²⁹, anti-PFR-A/C¹⁰⁵
1053 (1:1000), anti-Ty1¹⁰⁶ (1:250), anti-PAD1¹⁰⁷ (1:1000) and anti-RBP6⁴⁸ (1:1000).

1054

1055 **Indirect immunofluorescence analysis**

1056 For microscopic analysis, trypanosomes were either spread on glass slides
1057 and fixed in methanol for 5 min at -20°C or fixed in 2% PFA for 20 min at room
1058 temperature. Cellular DNA was visualized with 4',6-diamidino-2-phenylindole
1059 (DAPI; 1 µg/mL). Image acquisition was performed with a DeltaVision Elite
1060 widefield fluorescence microscope (GE Healthcare) equipped with a
1061 CoolSnap HQ2 CCD camera (Photometrics, Arizona, USA) and images were
1062 processed with ImageJ^{108,109}. Primary antibodies used are anti-CARP3
1063 (1:150), anti-Ty1 (1:100), anti-SAXO¹¹⁰ (mAB25; 1:25), anti-EP procyclin
1064 (cedarlane, cat. no. CLP001AP, 1:500), anti-calflagin¹¹¹ (1:1000).

1065

1066 **Live cell fluorescence microscopy**

1067 For live cell fluorescence microscopy, procyclic trypanosomes were
1068 resuspended in PBS and imaged using a DeltaVision Elite widefield
1069 fluorescence microscope (GE Healthcare) equipped with a CoolSnap HQ2
1070 CCD camera (Photometrics, Arizona, USA). Images were processed with
1071 ImageJ^{108,109}.

1072

1073 **Photoactivated localization microscopy**

1074 1.6 × 10⁷ trypanosomes were fixed in 2% PFA for 20 min at room
1075 temperature, washed 2-4 times with PBS/10 mM glycine and resuspended in
1076 50 µL PBS. 5 µL fixed cells were mixed with 1.5 µL (1:5000) 100 nm diameter
1077 fluorescent TetraSpeck Microbeads (Thermo Fisher Scientific) and 200 µL
1078 PBS and loaded into an 8 well glass bottom µ-slide (Ibidi, Martinsried,
1079 Germany). Slides were centrifuged for 10 min at 1400 × g and imaged on a

1080 Zeiss Elyra P.1 microscope (Carl Zeiss Microscopy GmbH, Jena, Germany)
1081 equipped with an Andor EM-CCD iXon DU 897 camera.
1082 PAmCherry was activated by an HR diode 50 mW 405 nm laser (Power
1083 linearly increased over the course of the experiment and dependent on the
1084 protein abundance) and excited via a 200 mW 561 nm OPSL laser line (15%
1085 power) (Emission filter: LP 570). The 405 line trigger was set to “none”
1086 (continuous conversion) while the 561 line trigger was set to “integration”
1087 (laser active only when the camera is collecting photons). MNeonGreen was
1088 excited via a 200 mW 488 nm OPSL laser line (15%) (no conversion required)
1089 (Emission filter: BP 495-590 + LP 750) (laser trigger set to “integration”).
1090 Fluorescent beads were bleached using a 561 nm laser at 100% power until
1091 the fluorescence level resided within the camera dynamic range. Both
1092 fluorescent tags were imaged in EPI mode (laser perpendicular to the sample)
1093 with an exposure time of 50 ms and an EMCCD gain of 200 (the experiment
1094 length depends of the protein abundance). 15 to 27 flagella were imaged per
1095 cell line. Peak fit, lateral drift and channel alignment were performed with ZEN
1096 Black (ZEN Black 2.1 SP3, version 14.0.4.201, 64-bit) while the follow up
1097 localization and colocalization analysis was performed via in house Fiji (Fiji is
1098 Just Image J¹⁰⁸) and R scripts (<http://www.R-project.org/>)
1099 (<https://github.com/GiacomoGiacomelli/Carp3-Co-localization-PALM>). For
1100 colocalization analysis, we used the coordinate-based colocalization (CBC)
1101 method of Malkusch, et al. ⁴². The CBC algorithm calculates a colocalization
1102 value for each molecule while taking into account the spatial distribution of the
1103 two populations within a user determined radius (R_{max}). All CBC values were

1104 calculated for six different R_{max} (50, 100, 200, 300, 400, 500 nm) and radius
1105 intervals of 5 nm (Extended Data Fig. 3a-f). The resulting colocalization
1106 parameter varies between +1 (perfectly correlated / high probability of
1107 colocalization), through 0 (non-correlated / low probability of colocalization) to
1108 -1 (anti-correlated / this value is of difficult interpretation)^{112,113}. As CBC
1109 values are expression of the relative distribution of the two protein
1110 populations, the values are influenced by the detection efficiency of each
1111 fluorescent tag. We therefore generated a control cell line with one *CARP3*
1112 allele fused to PAmCherry and the other *CARP3* allele fused to mNeonGreen.
1113 While both alleles were expressed at comparable levels, PALM imaging
1114 showed substantially more PAmCherry events compared to mNeonGreen
1115 events (Extended Data Fig. 2d). While mNeonGreen is suitable for PALM¹¹⁴, it
1116 is not photoactivatable and sample pre-bleaching is a necessary step for the
1117 collection of single molecule events. This results in permanent loss of a
1118 significant portion of the mNeonGreen population, hence altering the
1119 distribution of CBC values (Extended Data Fig. 2d). As CARP3 molecules are
1120 expected to colocalize with one another, we can use the obtained distribution
1121 of CBC values as a positive control for testing the remaining protein
1122 combinations. As a negative control, the CBC values' distribution for non-
1123 colocalizing proteins was obtained by simulating two independent Poisson
1124 point patterns (Extended Data Fig. 2f) via the "*rpoispp*" command¹¹⁵. The
1125 simulated point patterns were defined by a localization density (λ , expressed
1126 in localizations/nm²) and an area ("owin" class object – see¹¹⁵). Specifically,
1127 $\lambda_{PAmCherry}$ (0.00013 loc/nm²) and $\lambda_{mNeonGreen}$ (0.000026 loc/nm²) were

1128 chosen as to possess the same localization density as the protein populations
1129 from the positive control, while the area confining the simulation are
1130 comprised of a rectangular structure of 1 μm width and a total area equal to
1131 the total area from the positive control (broad approximation of a straight
1132 flagellum). The percentage of CBC values above or equal to 0.5
1133 (mNeonGreen to PAmCherry and vice versa) was determined and compared
1134 for increasing mNeonGreen concentrations (25, 50, 100, 200, 400 and 800
1135 molecules/ μm^2) and constant PAmCherry concentration at an R_{\max} of 300 nm
1136 and an interval width of 10 nm (Extended Data Fig. 3g,h). This analysis
1137 revealed highly similar values for $\text{CBC} \geq 0.5$ at the different mNeonGreen
1138 concentrations, excluding the necessity of separate negative controls for each
1139 fluorescent protein pair. The percentage of CBC values above or equal to 0.5
1140 of CARP3-PAmCherry / ACP1-mNG, CARP3-PAmCherry / calpain1.3-mNG,
1141 CARP3-PAmCherry / FLAM8-mNG and CARP3-PAmCherry / CARP3-mNG
1142 was compared to the percentage of CBC values above or equal to 0.5 in the
1143 negative control ($p < 0.05$, multiple comparison after Kruskal-Wallis, one
1144 tailed).

1145

1146 **Pull-down with cAMP agarose**

1147 3×10^8 procyclic *T. brucei* cells were washed twice with PBS and lysed in
1148 lysis buffer (10 mM Tris/Cl pH 7.5; 150 mM NaCl; 0.5 mM EDTA; 0.5% NP-40;
1149 Roche cOmplete protease inhibitor) for 30 min at 4°C. Lysates were
1150 incubated with plain agarose beads (Biolog Bremen) for 1 h at 4°C in order to
1151 remove proteins binding non-specifically to the bead matrix. Pull-downs were

1152 performed by incubation of the pre-cleared lysates with 60 μ L 2-AHA- or 8-
1153 AHA-agarose (Biolog Bremen Cat. No. A054, A028) beads slurry for 2 h at
1154 4°C, followed by five washes with lysis buffer. Bound proteins were eluted by
1155 boiling (5 min 95°) with 40 μ L 2× Laemmli sample buffer.

1156

1157 **Immunoprecipitations**

1158 Immunoprecipitation of CARP3 or of Ty1-tagged bait proteins was performed
1159 by binding anti-CARP3 or anti-Ty1 to magnetic protein A beads (Dynabeads,
1160 Invitrogen) followed by a 2-hour incubation with 1×10^8 trypanosomes lysed
1161 in lysis buffer (10 mM Tris/Cl pH 7.5; 150 mM NaCl; 0.5 mM EDTA; 0.5% NP-
1162 40; Roche cOmplete protease inhibitor) for 30 min at 4°C. Beads were
1163 washed 4x with lysis buffer and proteins were eluted by incubation with 50 μ L
1164 2× Laemmli sample buffer for 5 min at 95°C. Immunoprecipitations from
1165 HEK293T cells were carried out essentially using the same protocol with
1166 protein A sepharose beads and 5×10^5 cells.

1167

1168 **Enrichment and mass spectrometry analysis of CARP3-interacting or**
1169 **ESAG4-interacting proteins by GFP-trap pull-down**

1170 Immunoprecipitation of CARP3-YFP or ESAG4-GFP was performed using a
1171 GFP nanobody covalently coupled to magnetic agarose beads (GFP-trap)
1172 according to the manufacturer's instructions (Chromotek, Martinsried,
1173 Germany). Briefly, 2×10^8 *T. brucei* cells (for CARP3-YFP pull-down: AnTat
1174 1.1E wild type or CARP3-YFP, BSFs or PCFs, n = 2 replicates each; for
1175 ESAG4-GFP pull-down: MiTat 1.2 13-90 or ESAG4-GFP, BSFs, n = 2

replicates) were harvested by centrifugation, washed twice with serum-free culture medium and lysed in 1 mL lysis buffer (10 mM Tris/Cl pH 7.5; 150 mM NaCl; 0.5 mM EDTA; 0.4 % NP-40 (ESAG4-GFP) or 0.5% NP-40 (CARP3-YFP); Roche cOmplete protease inhibitor) for 30 min on ice. Soluble proteins were separated by centrifugation (10 min, 20,000 × g, 4°C) and incubated with GFP-trap beads (25 µL beads slurry) for 1h at 4°C on an overhead rotator. Beads were washed 4x with lysis buffer, followed by three washes with 50 mM Tris/Cl pH 8. Bound proteins were either eluted by boiling for 10 min with Laemmli sample buffer for SDS PAGE or beads with bound proteins were subjected to on-bead digest for mass spectrometry analysis. After on-bead digestion with trypsin, digested peptides were separated on an Ultimate 3000 RSLCnano (ThermoFisher) with a gradient from 4 to 40% acetonitrile in 0.1% formic acid over 40 min at 300 nL/min in a 15-cm analytical (75 µm ID home-packed with ReproSil-Pur C18-AQ 2.4 µm from Dr. Maisch). The effluent from the HPLC was directly electrosprayed into a Q Exactive HF instrument operated in data dependent mode to automatically switch between full scan MS and MS/MS acquisition. Survey full scan MS spectra (from m/z 250–1600) were acquired with resolution R = 60000 at m/z 400 (AGC target of 3x10⁶). The ten most intense peptide ions with charge states between 2 and 5 were sequentially isolated to a target value of 1x10⁵ and fragmented at 27% normalized collision energy. Typical mass spectrometric conditions were: spray voltage, 1.5 kV; no sheath and auxiliary gas flow; heated capillary temperature, 250°C; ion selection threshold, 33000 counts.

Protein identification and quantification (iBAQ) was performed using

1200 MaxQuant 1.6.3.4 (CARP3-YFP) or 1.6.14.0 (ESAG4-GFP)¹¹⁶ with the
1201 following parameters: Database, TriTrypDB-
1202 42_TbruceiTREU927_AnnotatedProteins (CARP3-YFP pull-down) or
1203 TriTrypDB-48_TbruceiLISTER427_AnnotatedProteins (ESAG4-GFP pull-
1204 down); MS tol, 10 ppm; MS/MS tol, 20 ppm; Peptide FDR, 0.1; Protein FDR,
1205 0.01 Min. peptide Length, 5; Variable modifications, Oxidation (M); Fixed
1206 modifications, Carbamidomethyl (C); Peptides for protein quantitation, razor
1207 and unique; Min. peptides, 1; Min. ratio count, 2. Statistical analysis was
1208 performed using Perseus 1.6.7.0¹¹⁷ with the following workflow: proteins only
1209 identified by site, reverse hits or potential contaminants were filtered out. For
1210 ESAG4-GFP pull downs, three replicate LC-MS/MS runs of each sample were
1211 grouped as technical replicates and the median thereof was used for further
1212 calculations. The iBAQ values of the remaining proteins were log₂
1213 transformed and missing values were replaced from normal distribution. Only
1214 proteins identified in both pull down replicates were considered for statistical
1215 evaluation with an FDR ≤ 0.05. The raw and processed mass spectrometry
1216 proteomics data have been deposited to the ProteomeXchange Consortium¹¹⁸
1217 (<http://proteomecentral.proteomexchange.org>) via the PRIDE partner
1218 repository¹¹⁹ with the dataset identifiers PXD025398 (CARP3-YFP) and
1219 PXD025412 (ESAG4-GFP), respectively.

1220

1221 **Proximity proteomics using CARP3 BiOID**

1222 BiOID was adapted from¹²⁰. Briefly, 4-5 × 10⁸ *T. brucei* MiTat 1.2 BSF cells
1223 expressing tetracycline-induced (1 µg/mL, 24 h) CARP3-BirA*-Ty1 or CARP3

1224 (control) were treated with 50 μ M biotin for 24 h (n = 3 replicates). Cells were
1225 harvested by centrifugation, washed 3x with PBS and lysed in 500 μ L lysis
1226 buffer (50 mM Tris/Cl pH 7.4; 500 mM NaCl; 5 mM EDTA; 0.4% SDS; 1 mM
1227 DTT; Roche cOmplete protease inhibitor) by sonication (Bioruptor; 2 cycles
1228 with 30" on/off, high energy). Triton X-100 was added to a final concentration
1229 of 2%, followed by sonication as above. Addition of 500 μ L Tris/Cl pH 7.4 was
1230 followed by another round of sonication. Soluble proteins were separated by
1231 centrifugation (15 min, 16,000 \times g, 4°C) and subjected to buffer exchange
1232 using a PD-10 column (GE Healthcare) according to the manufacturer's
1233 instructions. The eluate was concentrated (Spin-X UF 6 concentrator column)
1234 to < 1mL and incubated with 50 μ L streptavidin-coupled magnetic beads
1235 (Dynabeads ® MyOne™ Streptavidin T1, ThermoFisher) overnight at 4°C on
1236 an overhead rotator. Beads were washed 5x with PBS, followed by elution
1237 with Laemmli sample buffer for 10 min at 95°C. Sample preparation for mass
1238 spectrometry, protein digestion and LC-MS parameters used for nanoLC-
1239 MS/MS analysis on a nanospray Q Exactive were previously described²⁴.
1240 Raw spectra were analyzed with MaxQuant version 1.6.17.0¹¹⁶, which
1241 incorporates the Andromeda search engine, using the *Trypanosoma brucei*
1242 TriTrypDB-51_TbruceiTREU927 protein database and the following settings:
1243 three missed cleavages from trypsin digestion were allowed;
1244 carbamidomethyl-cysteine was set as fixed modification and biotinylation (K),
1245 oxidation (M), acetylation (protein N-terminal) and deamidation (N, Q) were
1246 set as dynamic modifications. The MaxQuant output was loaded into Perseus
1247 version 1.6.7.0¹¹⁷ and filtered to exclude proteins 'only identified by site',

1248 reverse hits and potential contaminants. The LFQ values of the remaining
1249 proteins were \log_2 transformed and missing values were replaced from normal
1250 distribution. Only proteins identified in all three pull-downs were considered for
1251 further analysis. Proteins were considered as statistically significant with FDR
1252 ≤ 0.05 and $s_0 = 2$ (two-sided Student's T-test). The raw and processed mass
1253 spectrometry proteomics data have been deposited to the ProteomeXchange
1254 Consortium¹¹⁸ (<http://proteomecentral.proteomexchange.org>) via the PRIDE
1255 partner repository¹¹⁹ with the dataset identifier PXD025357.

1256

1257 **Quantitative proteomics upon CARP3 knock-down**

1258 3×10^7 *T. brucei* MiTat 1.2 13-90 BSF cells with tetracycline-inducible *CARP3*
1259 RNAi knock-down were induced or not with 5 $\mu\text{g}/\text{mL}$ tetracycline for 24 h (n =
1260 4 replicates). Cell lysis, protein digestion, peptide purification and MS/MS
1261 analysis were performed as described by Humphrey et al.¹²¹. Purified
1262 peptides were injected in an RSLChano system (Thermo) and separated in a
1263 25-cm analytical Aurora C18 nanocolumn (75 μm ID 120 Å, 1.6 μm , Ion
1264 Opticks) with a 120-min gradient from 4 to 40% acetonitrile in 0.1% formic
1265 acid. The effluent from the HPLC was directly electrosprayed into a Q
1266 Exactive HF (Thermo), operated in data dependent mode to automatically
1267 switch between full scan MS and MS/MS acquisition. Survey full scan MS
1268 spectra (from m/z 375–1600) were acquired with resolution R = 60000 at m/z
1269 400 (AGC target of 3×10^6). The ten most intense peptide ions with charge
1270 states between 3 and 5 were sequentially isolated to a target value of 1×10^5
1271 and fragmented at 27% normalized collision energy. Typical mass

1272 spectrometric conditions were: spray voltage, 1.5 kV; no sheath and auxiliary
1273 gas flow; heated capillary temperature, 250°C; ion selection threshold, 33000
1274 counts.

1275 Protein identification and quantification (LFQ) was performed using MaxQuant
1276 version 1.6.10.43¹¹⁶ with the following parameters: Database, TriTrypDB-
1277 46_TbruceiTREU927_AnnotatedProteins; MS tol, 10 ppm; MS/MS tol, 20
1278 ppm; Peptide FDR, 0.1; Protein FDR, 0.01 Min. peptide Length, 5; Variable
1279 modifications, Oxidation (M); Fixed modifications, Carbamidomethyl (C);
1280 Peptides for protein quantitation, razor and unique; Min. peptides, 1; Min. ratio
1281 count, 2. Statistical analysis was performed using Perseus 1.6.7.0¹¹⁷ with the
1282 following workflow: proteins only identified by site, reverse hits or potential
1283 contaminants were filtered out. Only proteins that were identified in at least
1284 three of the four non-induced replicate samples were considered for further
1285 analysis. The LFQ values of the remaining proteins were log₂ transformed and
1286 missing values were replaced from normal distribution. Statistical significance
1287 was evaluated with a two-sided Student's t-test with FDR ≤ 0.05 and s₀ = 0.1.
1288 The raw and processed mass spectrometry proteomics data have been
1289 deposited to the ProteomeXchange Consortium¹¹⁸
1290 (<http://proteomecentral.proteomexchange.org>) via the PRIDE partner
1291 repository¹¹⁹ with the dataset identifier PXD025401.

1292

1293 **Tsetse fly infections and imaging of isolated parasites**

1294 Fly infection experiments for *flam8* KO and *in situ* *FLAM8* rescue:

1295 As previously described¹²², *Glossina morsitans morsitans* tsetse flies were
1296 maintained in the Trypanosome Transmission Group's insectarium of the
1297 Institut Pasteur at 27°C with 70% relative humidity. Flies were kept in
1298 Roubaud cages and fed through an artificial membrane feeding system with
1299 fresh mechanically defibrinated sheep blood three times a week. Batches of
1300 50 teneral males (unfed adults emerged from their puparium since 12 h to 72
1301 h) were allowed to ingest parasites in SDM79 medium supplemented with
1302 10% fetal calf serum and 10 mM L-glutathione.

1303 Flies were starved for at least 48 h before dissection. Four weeks after
1304 infection, all living flies were dissected: salivary glands were first rapidly
1305 isolated in a drop of PBS, the whole tsetse alimentary tract was then arranged
1306 lengthways and the foregut and proventriculus were physically separated from
1307 the midgut in distinct PBS drops. The infection was scrutinized in the posterior
1308 and anterior midgut (PMG and AMG), in the cardia or proventriculus (PV) and
1309 foregut, as well as in the salivary glands (SG). The relative parasite densities
1310 per organ were evaluated by eye scoring under a 40× objective using the
1311 following scale: 0 for no parasites, 1 for 1 to 10 parasites, 2 for 10 to 100, 3 for
1312 100 to 1000 and 4 for >1000 parasites per microscopic field, as described in
1313 Schuster et al.¹¹. Then, tissues were dilacerated to allow parasites to spread
1314 in PBS and parasites were recovered and treated for further experiments no
1315 more than 15 min after dissection. For immunofluorescence, parasites were
1316 rapidly allowed to settle on poly-lysine coated slides until drying. Cells were
1317 fixed for 10 sec in methanol at -20°C and re-hydrated in PBS during 10 min.
1318 Slides were then incubated for 45 min at 37°C with the anti-FLAM8 (1:500)

1319 and anti-CARP3 (1:150) primary antibody in PBS with 0,1% bovine serum
1320 albumin. Slides were washed in PBS and incubated for 30 min at 37°C with
1321 the appropriate subclass-specific secondary antibodies coupled to Alexa Fluor
1322 488 (Invitrogen) or Cy3 (Jackson ImmunoResearch). Slides were then stained
1323 with DAPI for visualization of their kinetoplast and nuclear DNA contents and
1324 mounted under coverslip with Prolong antifade reagent (Invitrogen). Slides
1325 were finally observed with a DMI4000 epifluorescence microscope (Leica) and
1326 images were captured with an Orca 03-G camera (Hamamatsu). Pictures
1327 were acquired with Micro-Manager 1.4 and prepared with ImageJ 1.8.0 (NIH).

1328 Antwerp fly infection experiments for carp3 KO and *in situ* CARP3 rescue:
1329 Freshly emerged tsetse flies (*Glossina morsitans morsitans* – Institute of
1330 Tropical Medicine Antwerp colony; 24-48 hours after emergence) were fed
1331 their first blood meal on fresh defibrinated horse blood containing bloodstream
1332 forms from either the *T. brucei*AnTat 1.1 WT, the *carp3* KO (two independent
1333 clones KO1 and KO2) or an *in situ* CARP3 rescue clone (resc1),
1334 supplemented with 10 mM reduced L-glutathione, as described in ¹²³. For this,
1335 bloodstream parasites present in the blood of cyclophosphamide-
1336 immunosuppressed mice (Endoxan) (ITM Animal Ethics Committee clearance
1337 nr. VPU2014-1) at 6–7 days post-infection were mixed with defibrinated horse
1338 blood to obtain around 10⁶ parasites/ml in the initial tsetse fly blood meal.
1339 Flies were further fed every 2–3 days on uninfected defibrinated horse blood.
1340 At a defined period after infection, all living flies were dissected after at least
1341 48 hours of starvation, and different tissues were examined for parasite
1342 presence/density by phase-contrast microscopy. To determine in a first

1343 experiment the overall tsetse infection rates for the different cell lines, midgut
1344 and salivary glands were examined five weeks after infection. Then, to
1345 estimate in more detail the infection rates and the parasite density in the
1346 posterior & anterior midgut and proventriculus, flies were dissected three
1347 weeks after the initial infective bloodmeal (without the supplement of L-
1348 glutathione). Parasite abundance was scored using the aforementioned
1349 method of Schuster, et al. ¹¹.

1350

1351 **Structural modeling of AC and CARP3 proteins**

1352 Structural modeling of CARP3 (Extended Data Fig. 1) and ESAG4 (Extended
1353 Data Fig. 8) was initially carried out using the ColabFold notebook
1354 AlphaFold2_Advanced
1355 (https://colab.research.google.com/github/sokrypton/ColabFold/blob/main/beta/AlphaFold2_advanced.ipynb) utilizing the MMseqs2 database for generating
1356 multiple sequence alignments (MSA)¹²⁴. Structural models were later
1357 confirmed by executing the originally released AlphaFold2 code along with the
1358 full sequence databases³⁷ using an installation on a local high-performing
1359 cluster. Although CARP3 is trypanosome-specific, AlphaFold2 retrieved 34
1360 unique sequence homologs for generating the MSA, which is just above the
1361 alignment depth cut-off of 30 sequences below which the model accuracy was
1362 found to decrease significantly³⁷. Models of CARP3-AC complexes shown in
1363 Extended Data Fig. 8 were generated using AlphaFold Colab
1364 (<https://colab.research.google.com/github/deepmind/alphafold/blob/main/notebooks/AlphaFold.ipynb>), a slightly simplified version of AlphaFold v. 2.1.0

1367 trained on oligomeric protein structures for improved prediction of protein
1368 complexes⁵⁰. AlphaFold Colab was also used to produce a model of homo-
1369 dimeric ESAG4 bound to CARP3 as shown in Fig. 6e. All superpositioning
1370 and figures of protein structures were created in PyMOL (*The PyMOL
1371 Molecular Graphics System, version 2.5* Schrödinger, LLC.).

1372

1373

1374 **Data availability**

1375 The proteomics datasets are available in the PRIDE partner repository with
1376 the dataset identifiers PXD025398 (CARP3-YFP pull down), PXD025412
1377 (ESAG4-GFP pull down), PXD025357 (CARP3 BioID) and PXD025401
1378 (CARP3 RNAi quantitative proteomics).

1379

1380

1381 **Code availability**

1382 R scripts for colocalization analysis of PALM data are available at
1383 (<https://github.com/GiacomoGiacomelli/Carp3-Co-localization-PALM>).

1384

1385

1386

1387

1388

1389

1390

1391 **References**

1392

- 1393 1 Zuzarte-Luís, V. & Mota, M. M. Parasite Sensing of Host Nutrients and Environmental
1394 Cues. *Cell Host & Microbe* **23**, 749-758,
1395 doi:<https://doi.org/10.1016/j.chom.2018.05.018> (2018).
- 1396 2 Landfear, S. M. & Zilberstein, D. Sensing What's Out There - Kinetoplastid Parasites.
1397 *Trends in parasitology* **35**, 274-277, doi:10.1016/j.pt.2018.12.004 (2019).
- 1398 3 Walsh, B. & Hill, K. L. Right place, right time: Environmental sensing and signal
1399 transduction directs cellular differentiation and motility in *Trypanosoma brucei*.
1400 *Molecular microbiology* **115**, 930-941, doi:<https://doi.org/10.1111/mmi.14682> (2021).
- 1401 4 Brun, R., Blum, J., Chappuis, F. & Burri, C. Human African trypanosomiasis. *Lancet*
1402 **375**, 148-159, doi:10.1016/s0140-6736(09)60829-1 (2010).
- 1403 5 Oberholzer, M., Lopez, M. A., McLelland, B. T. & Hill, K. L. Social Motility in African
1404 Trypanosomes. *PLoS Pathogens* **6**, e1000739, doi:10.1371/journal.ppat.1000739
1405 (2010).
- 1406 6 Kearns, D. B. A field guide to bacterial swarming motility. *Nature reviews.*
1407 *Microbiology* **8**, 634-644, doi:10.1038/nrmicro2405 (2010).
- 1408 7 Lopez, M. A., Saada, E. A. & Hill, K. L. Insect stage-specific adenylate cyclases
1409 regulate social motility in African trypanosomes. *Eukaryot Cell* **14**, 104-112,
1410 doi:10.1128/ec.00217-14 (2015).
- 1411 8 Oberholzer, M., Saada, E. A. & Hill, K. L. Cyclic AMP Regulates Social Behavior in
1412 African Trypanosomes. *mBio* **6**, doi:10.1128/mBio.01954-14 (2015).
- 1413 9 Shaw, S. *et al.* Flagellar cAMP signaling controls trypanosome progression through
1414 host tissues. *Nat Commun* **10**, 803, doi:10.1038/s41467-019-08696-y (2019).
- 1415 10 Rose, C. *et al.* *Trypanosoma brucei* colonizes the tsetse gut via an immature
1416 peritrophic matrix in the proventriculus. *Nat Microbiol*, doi:10.1038/s41564-020-0707-
1417 z (2020).

- 1418 11 Schuster, S. *et al.* Developmental adaptations of trypanosome motility to the tsetse fly
1419 host environments unravel a multifaceted in vivo microswimmer system. *eLife* **6**,
1420 doi:10.7554/eLife.27656 (2017).
- 1421 12 Balbach, M., Beckert, V., Hansen, J. N. & Wachten, D. Shedding light on the role of
1422 cAMP in mammalian sperm physiology. *Mol Cell Endocrinol* **468**, 111-120,
1423 doi:10.1016/j.mce.2017.11.008 (2018).
- 1424 13 Langousis, G. & Hill, K. L. Motility and more: the flagellum of *Trypanosoma brucei*.
1425 *Nature reviews. Microbiology* **12**, 505-518, doi:10.1038/nrmicro3274 (2014).
- 1426 14 Liu, W., Apagyi, K., McLeavy, L. & Ersfeld, K. Expression and cellular localisation of
1427 calpain-like proteins in *Trypanosoma brucei*. *Molecular and biochemical parasitology*
1428 **169**, 20-26, doi:10.1016/j.molbiopara.2009.09.004 (2010).
- 1429 15 Subota, I. *et al.* Proteomic analysis of intact flagella of procyclic *Trypanosoma brucei*
1430 cells identifies novel flagellar proteins with unique sub-localization and dynamics.
1431 *Molecular & cellular proteomics : MCP* **13**, 1769-1786,
1432 doi:10.1074/mcp.M113.033357 (2014).
- 1433 16 Varga, V., Moreira-Leite, F., Portman, N. & Gull, K. Protein diversity in discrete
1434 structures at the distal tip of the trypanosome flagellum. *Proceedings of the National
1435 Academy of Sciences of the United States of America* **114**, E6546-e6555,
1436 doi:10.1073/pnas.1703553114 (2017).
- 1437 17 Vélez-Ramírez, D. E. *et al.* APEX2 Proximity Proteomics Resolves Flagellum
1438 Subdomains and Identifies Flagellum Tip-Specific Proteins in *Trypanosoma brucei*.
1439 *mSphere* **6**, doi:10.1128/mSphere.01090-20 (2021).
- 1440 18 Saada, E. A. *et al.* Insect Stage-Specific Receptor Adenylate Cyclases Are Localized
1441 to Distinct Subdomains of the *Trypanosoma brucei* Flagellar Membrane. *Eukaryotic
1442 Cell* **13**, 1064-1076, doi:10.1128/EC.00019-14 (2014).
- 1443 19 Buxton, I. L. & Brunton, L. L. Compartments of cyclic AMP and protein kinase in
1444 mammalian cardiomyocytes. *The Journal of biological chemistry* **258**, 10233-10239
1445 (1983).

- 1446 20 Zaccolo, M., Zerio, A. & Lobo, M. J. Subcellular Organization of the cAMP Signaling
1447 Pathway. *Pharmacol Rev* **73**, 278-309, doi:10.1124/pharmrev.120.000086 (2021).
- 1448 21 Schou, K. B., Pedersen, L. B. & Christensen, S. T. Ins and outs of GPCR signaling in
1449 primary cilia. *EMBO reports* **16**, 1099-1113,
1450 doi:<https://doi.org/10.15252/embr.201540530> (2015).
- 1451 22 Tschaikner, P., Enzler, F., Torres-Quesada, O., Aanstad, P. & Stefan, E. Hedgehog
1452 and Gpr161: Regulating cAMP Signaling in the Primary Cilium. *Cells* **9**, 118,
1453 doi:10.3390/cells9010118 (2020).
- 1454 23 Schleicher, K. & Zaccolo, M. Defining a cellular map of cAMP nanodomains. *Mol
1455 Pharmacol*, mol.119.118869, doi:10.1124/mol.119.118869 (2020).
- 1456 24 Bachmaier, S. *et al.* Nucleoside analogue activators of cyclic AMP-independent
1457 protein kinase A of *Trypanosoma*. *Nature Communications* **10**, 1421,
1458 doi:10.1038/s41467-019-09338-z (2019).
- 1459 25 Makin, L. & Gluenz, E. cAMP signalling in trypanosomatids: role in pathogenesis and
1460 as a drug target. *Trends in Parasitology* **31**, 373-379, doi:10.1016/j.pt.2015.04.014
1461 (2015).
- 1462 26 Salmon, D. Adenylate Cyclases of *Trypanosoma brucei*, Environmental Sensors and
1463 Controllers of Host Innate Immune Response. *Pathogens (Basel, Switzerland)* **7**, 48,
1464 doi:10.3390/pathogens7020048 (2018).
- 1465 27 de Koning, H. P. *et al.* Pharmacological validation of *Trypanosoma brucei*
1466 phosphodiesterases as novel drug targets. *The Journal of infectious diseases* **206**,
1467 229-237, doi:10.1093/infdis/jir857 (2012).
- 1468 28 Oberholzer, M. *et al.* The *Trypanosoma brucei* cAMP phosphodiesterases TbrPDEB1
1469 and TbrPDEB2: flagellar enzymes that are essential for parasite virulence. *FASEB
1470* **21**, 720-731 (2007).
- 1471 29 Salmon, D. *et al.* Cytokinesis of *Trypanosoma brucei* bloodstream forms depends on
1472 expression of adenylyl cyclases of the ESAG4 or ESAG4-like subfamily. *Molecular
1473 microbiology* **84**, 225-242, doi:10.1111/j.1365-2958.2012.08013.x (2012).

- 1474 30 Gould, M. K. *et al.* Cyclic AMP effectors in African trypanosomes revealed by
1475 genome-scale RNA interference library screening for resistance to the
1476 phosphodiesterase inhibitor CpdA. *Antimicrobial agents and chemotherapy* **57**, 4882-
1477 4893, doi:10.1128/AAC.00508-13 (2013).
- 1478 31 Salmon, D. *et al.* Adenylate cyclases of *Trypanosoma brucei* inhibit the innate
1479 immune response of the host. *Science (New York, N.Y.)* **337**, 463-466,
1480 doi:10.1126/science.1222753 (2012).
- 1481 32 Hertz-Fowler, C. *et al.* Telomeric Expression Sites Are Highly Conserved in
1482 *Trypanosoma brucei*. *PLOS ONE* **3**, e3527, doi:10.1371/journal.pone.0003527
1483 (2008).
- 1484 33 Rotureau, B. & Van Den Abbeele, J. Through the dark continent: African
1485 trypanosome development in the tsetse fly. *Frontiers in Cellular and Infection*
1486 *Microbiology* **3**, 53, doi:10.3389/fcimb.2013.00053 (2013).
- 1487 34 Savage, A. F. *et al.* Transcriptome Profiling of *Trypanosoma brucei* Development in
1488 the Tsetse Fly Vector *Glossina morsitans*. *PLoS ONE* **11**, e0168877,
1489 doi:10.1371/journal.pone.0168877 (2016).
- 1490 35 Naguleswaran, A. *et al.* Developmental changes and metabolic reprogramming
1491 during establishment of infection and progression of *Trypanosoma brucei brucei*
1492 through its insect host. *bioRxiv*, 2021.2005.2026.445766,
1493 doi:10.1101/2021.05.26.445766 (2021).
- 1494 36 Dyer, N. A., Rose, C., Ejeh, N. O. & Acosta-Serrano, A. Flying tryps: survival and
1495 maturation of trypanosomes in tsetse flies. *Trends Parasitol* **29**, 188-196,
1496 doi:10.1016/j.pt.2013.02.003 (2013).
- 1497 37 Jumper, J. *et al.* Highly accurate protein structure prediction with AlphaFold. *Nature*
1498 **596**, 583-589, doi:10.1038/s41586-021-03819-2 (2021).
- 1499 38 Lopez, M. A., Nguyen, H. T., Oberholzer, M. & Hill, K. L. Social parasites. *Current*
1500 *Opinion in Microbiology* **14**, 642-648, doi:<https://doi.org/10.1016/j.mib.2011.09.012>
1501 (2011).

- 1502 39 Bachmaier, S., Thanner, T. & Boshart, M. Culturing and Transfection of Pleomorphic
1503 *Trypanosoma brucei*. *Methods in molecular biology (Clifton, N.J.)* **2116**, 23-38,
1504 doi:10.1007/978-1-0716-0294-2_2 (2020).
- 1505 40 Dean, S., Sunter, J. D. & Wheeler, R. J. TrypTag.org: A Trypanosome Genome-wide
1506 Protein Localisation Resource. *Trends in parasitology* **33**, 80-82,
1507 doi:10.1016/j.pt.2016.10.009 (2017).
- 1508 41 Aksoy, S., Weiss, B. & Attardo, G. Paratransgenesis applied for control of tsetse
1509 transmitted sleeping sickness. *Advances in experimental medicine and biology* **627**,
1510 35-48, doi:10.1007/978-0-387-78225-6_3 (2008).
- 1511 42 Malkusch, S. *et al.* Coordinate-based colocalization analysis of single-molecule
1512 localization microscopy data. *Histochemistry and cell biology* **137**, 1-10,
1513 doi:10.1007/s00418-011-0880-5 (2012).
- 1514 43 Emmer, B. T., Maric, D. & Engman, D. M. Molecular mechanisms of protein and lipid
1515 targeting to ciliary membranes. *Journal of cell science* **123**, 529,
1516 doi:10.1242/jcs.062968 (2010).
- 1517 44 Kelly, F. D., Sanchez, M. A. & Landfear, S. M. Touching the Surface: Diverse Roles
1518 for the Flagellar Membrane in Kinetoplastid Parasites. *Microbiology and Molecular
1519 Biology Reviews* **84**, e00079-00019, doi:10.1128/mmbr.00079-19 (2020).
- 1520 45 Wright, M. H., Paape, D., Price, H. P., Smith, D. F. & Tate, E. W. Global Profiling and
1521 Inhibition of Protein Lipidation in Vector and Host Stages of the Sleeping Sickness
1522 Parasite *Trypanosoma brucei*. *ACS Infectious Diseases* **2**, 427-441,
1523 doi:10.1021/acsinfecdis.6b00034 (2016).
- 1524 46 Calvo-Alvarez, E., Crouzols, A. & Rotureau, B. FLAgellum Member 8 modulates
1525 extravascular trypanosome distribution in the mammalian host. *bioRxiv*,
1526 2021.2001.2008.425862, doi:10.1101/2021.01.08.425862 (2021).
- 1527 47 Calvo-Alvarez, E., Cren-Travaille, C., Crouzols, A. & Rotureau, B. A new chimeric
1528 triple reporter fusion protein as a tool for in vitro and in vivo multimodal imaging to
1529 monitor the development of African trypanosomes and *Leishmania* parasites.
1530 *Infection, genetics and evolution : journal of molecular epidemiology and evolutionary*

- 1531 *genetics in infectious diseases* **63**, 391-403, doi:10.1016/j.meegid.2018.01.011
1532 (2018).
- 1533 48 Kolev, N. G., Ramey-Butler, K., Cross, G. A. M., Ullu, E. & Tschudi, C.
1534 Developmental Progression to Infectivity in *Trypanosoma brucei* Triggered by an
1535 RNA-Binding Protein. *Science (New York, N.Y.)* **338**, 1352-1353,
1536 doi:10.1126/science.1229641 (2012).
- 1537 49 Chiasson, D. *et al.* A unified multi-kingdom Golden Gate cloning platform. *Scientific
1538 reports* **9**, 10131, doi:10.1038/s41598-019-46171-2 (2019).
- 1539 50 Evans, R. *et al.* Protein complex prediction with AlphaFold-Multimer. *bioRxiv*,
1540 2021.2010.2004.463034, doi:10.1101/2021.10.04.463034 (2021).
- 1541 51 Goldston, A. M., Sharma, A. I., Paul, K. S. & Engman, D. M. Acylation in
1542 trypanosomatids: an essential process and potential drug target. *Trends in
1543 parasitology* **30**, 350-360, doi:10.1016/j.pt.2014.05.003 (2014).
- 1544 52 Wright, M. H., Heal, W. P., Mann, D. J. & Tate, E. W. Protein myristoylation in health
1545 and disease. *Journal of chemical biology* **3**, 19-35, doi:10.1007/s12154-009-0032-8
1546 (2009).
- 1547 53 Emmer, B. T. *et al.* Global Analysis of Protein Palmitoylation in African
1548 Trypanosomes. *Eukaryotic Cell* **10**, 455, doi:10.1128/EC.00248-10 (2011).
- 1549 54 Sharma, A. I. *et al.* Sterol targeting drugs reveal life cycle stage-specific differences in
1550 trypanosome lipid rafts. *Scientific reports* **7**, 9105, doi:10.1038/s41598-017-08770-9
1551 (2017).
- 1552 55 Sharma, A. I., Olson, C. L. & Engman, D. M. The Lipid Raft Proteome of African
1553 Trypanosomes Contains Many Flagellar Proteins. *Pathogens (Basel, Switzerland)* **6**,
1554 doi:10.3390/pathogens6030039 (2017).
- 1555 56 Cooper, Dermot M. F. & Tabbasum, Valentina G. Adenylate cyclase-centred
1556 microdomains. *Biochemical Journal* **462**, 199-213, doi:10.1042/BJ20140560 %J
1557 Biochemical Journal (2014).

- 1558 57 Bieger, B. & Essen, L. O. Structural analysis of adenylate cyclases from
1559 *Trypanosoma brucei* in their monomeric state. *Embo j* **20**, 433-445,
1560 doi:10.1093/emboj/20.3.433 (2001).
- 1561 58 Paindavoine, P. *et al.* A gene from the variant surface glycoprotein expression site
1562 encodes one of several transmembrane adenylate cyclases located on the flagellum
1563 of *Trypanosoma brucei*. *Mol Cell Biol* **12**, 1218-1225, doi:10.1128/mcb.12.3.1218-
1564 1225.1992 (1992).
- 1565 59 Rolin, S. *et al.* Stage-specific adenylate cyclase activity in *Trypanosoma brucei*. *Exp
1566 Parasitol* **71**, 350-352, doi:10.1016/0014-4894(90)90041-a (1990).
- 1567 60 Voorheis, H. P. & Martin, B. R. Characteristics of the calcium-mediated mechanism
1568 activating adenylate cyclase in *Trypanosoma brucei*. *Eur J Biochem* **116**, 471-477,
1569 doi:10.1111/j.1432-1033.1981.tb05360.x (1981).
- 1570 61 Su, Q., Mehta, S. & Zhang, J. Liquid-liquid phase separation: Orchestrating cell
1571 signaling through time and space. *Molecular Cell* **81**, 4137-4146,
1572 doi:10.1016/j.molcel.2021.09.010 (2021).
- 1573 62 Calvo-Alvarez, E. *et al.* Redistribution of FLAGellar Member 8 during the trypanosome
1574 life cycle: Consequences for cell fate prediction. *Cell Microbiol* **23**, e13347,
1575 doi:10.1111/cmi.13347 (2021).
- 1576 63 Fort, C., Bonnefoy, S., Kohl, L. & Bastin, P. Intraflagellar transport is required for the
1577 maintenance of the trypanosome flagellum composition but not its length. *Journal of
1578 cell science* **129**, 3026-3041, doi:10.1242/jcs.188227 (2016).
- 1579 64 Shaw, S. *et al.* Cyclic AMP signalling and glucose metabolism mediate pH taxis by
1580 African trypanosomes. *bioRxiv*, 2021.2001.2001.424252,
1581 doi:10.1101/2021.01.01.424252 (2021).
- 1582 65 Imhof, S. & Roditi, I. The Social Life of African Trypanosomes. *Trends Parasitol* **31**,
1583 490-498, doi:10.1016/j.pt.2015.06.012 (2015).
- 1584 66 Herder, S. *et al.* *Trypanosoma brucei* 29-13 strain is inducible in but not permissive
1585 for the tsetse fly vector. *Exp Parasitol* **117**, 111-114,
1586 doi:10.1016/j.exppara.2007.05.011 (2007).

- 1587 67 Peacock, L., Ferris, V., Bailey, M. & Gibson, W. Fly transmission and mating of
1588 *Trypanosoma brucei brucei* strain 427. *Molecular and biochemical parasitology* **160**,
1589 100-106, doi:10.1016/j.molbiopara.2008.04.009 (2008).
- 1590 68 Schuster, S. *et al.* Unexpected plasticity in the life cycle of *Trypanosoma brucei*. *eLife*
1591 **10**, doi:10.7554/eLife.66028 (2021).
- 1592 69 Vickerman, K., Tetley, L., Hendry, K. A. & Turner, C. M. Biology of African
1593 trypanosomes in the tsetse fly. *Biol Cell* **64**, 109-119, doi:10.1016/0248-
1594 4900(88)90070-6 (1988).
- 1595 70 Krüger, T., Maus, K., Kreß, V., Meyer-Natus, E. & Engstler, M. Single-cell motile
1596 behaviour of *Trypanosoma brucei* in thin-layered fluid collectives. *The European*
1597 *Physical Journal E* **44**, 37, doi:10.1140/epje/s10189-021-00052-7 (2021).
- 1598 71 DeMarco, S. F., Saada, E. A., Lopez, M. A. & Hill, K. L. Identification of Positive
1599 Chemotaxis in the Protozoan Pathogen *Trypanosoma brucei*. *mSphere* **5**,
1600 doi:10.1128/mSphere.00685-20 (2020).
- 1601 72 Schwede, A., Macleod, O. J., MacGregor, P. & Carrington, M. How Does the VSG
1602 Coat of Bloodstream Form African Trypanosomes Interact with External Proteins?
1603 *PLoS Pathog* **11**, e1005259, doi:10.1371/journal.ppat.1005259 (2015).
- 1604 73 Heldin, C.-H., Lu, B., Evans, R. & Gutkind, J. S. Signals and Receptors. *Cold Spring*
1605 *Harb Perspect Biol* **8**, a005900-a005900, doi:10.1101/cshperspect.a005900 (2016).
- 1606 74 Nolan, D. P., Rolin, S., Rodriguez, J. R., Van Den Abbeele, J. & Pays, E. Slender and
1607 stumpy bloodstream forms of *Trypanosoma brucei* display a differential response to
1608 extracellular acidic and proteolytic stress. *Eur J Biochem* **267**, 18-27,
1609 doi:10.1046/j.1432-1327.2000.00935.x (2000).
- 1610 75 Rolin, S. *et al.* Simultaneous but independent activation of adenylate cyclase and
1611 glycosylphosphatidylinositol-phospholipase C under stress conditions in
1612 *Trypanosoma brucei*. *The Journal of biological chemistry* **271**, 10844-10852,
1613 doi:10.1074/jbc.271.18.10844 (1996).

- 1614 76 Lander, N., Chiurillo, M. A. & Docampo, R. Signaling pathways involved in
1615 environmental sensing in *Trypanosoma cruzi*. *Molecular microbiology* **115**, 819-828,
1616 doi:<https://doi.org/10.1111/mmi.14621> (2021).
- 1617 77 Ellison, C. & Brun, Y. V. Mechanosensing: a regulation sensation. *Curr Biol* **25**, R113-
1618 R115, doi:10.1016/j.cub.2014.12.026 (2015).
- 1619 78 Dave, N. *et al.* A novel mechanosensitive channel controls osmoregulation,
1620 differentiation, and infectivity in *Trypanosoma cruzi*. *eLife* **10**, e67449,
1621 doi:10.7554/eLife.67449 (2021).
- 1622 79 Wang, S. C., Lin, J. T. & Chern, Y. Novel regulation of adenylyl cyclases by direct
1623 protein-protein interactions: insights from snapin and ric8a. *Neuro-Signals* **17**, 169-
1624 180, doi:10.1159/000200076 (2009).
- 1625 80 Bahn, Y. S. & Sundstrom, P. CAP1, an adenylate cyclase-associated protein gene,
1626 regulates bud-hypha transitions, filamentous growth, and cyclic AMP levels and is
1627 required for virulence of *Candida albicans*. *J Bacteriol* **183**, 3211-3223,
1628 doi:10.1128/JB.183.10.3211-3223.2001 (2001).
- 1629 81 Hu, W. *et al.* The complex of TRIP-Br1 and XIAP ubiquitinates and degrades multiple
1630 adenylyl cyclase isoforms. *eLife* **6**, e28021, doi:10.7554/eLife.28021 (2017).
- 1631 82 Chung, W. L., Leung, K. F., Carrington, M. & Field, M. C. Ubiquitylation is required for
1632 degradation of transmembrane surface proteins in trypanosomes. *Traffic*
1633 (*Copenhagen, Denmark*) **9**, 1681-1697, doi:10.1111/j.1600-0854.2008.00785.x
1634 (2008).
- 1635 83 Zoltner, M., Leung, K. F., Alsford, S., Horn, D. & Field, M. C. Modulation of the
1636 Surface Proteome through Multiple Ubiquitylation Pathways in African
1637 Trypanosomes. *PLOS Pathogens* **11**, e1005236, doi:10.1371/journal.ppat.1005236
1638 (2015).
- 1639 84 Naula, C., Schaub, R., Leech, V., Melville, S. & Seebeck, T. Spontaneous
1640 dimerization and leucine-zipper induced activation of the recombinant catalytic
1641 domain of a new adenylyl cyclase of *Trypanosoma brucei*, GRESAG4.4B. *Molecular*

- 1642 *and biochemical parasitology* **112**, 19-28, doi:10.1016/s0166-6851(00)00338-8
1643 (2001).
- 1644 85 Morton, D. B. & Anderson, E. J. MsGC-beta3 forms active homodimers and inactive
1645 heterodimers with NO-sensitive soluble guanylyl cyclase subunits. *J Exp Biol* **206**,
1646 937-947, doi:10.1242/jeb.00160 (2003).
- 1647 86 Vallin, B. *et al.* Novel short isoforms of adenylyl cyclase as negative regulators of
1648 cAMP production. *Biochimica et Biophysica Acta (BBA) - Molecular Cell Research*
1649 **1865**, 1326-1340, doi:<https://doi.org/10.1016/j.bbamcr.2018.06.012> (2018).
- 1650 87 Vassella, E., Reuner, B., Yutzy, B. & Boshart, M. Differentiation of African
1651 trypanosomes is controlled by a density sensing mechanism which signals cell cycle
1652 arrest via the cAMP pathway. *Journal of cell science* **110** (Pt 21), 2661-2671 (1997).
- 1653 88 Vassella, E. & Boshart, M. High molecular mass agarose matrix supports growth of
1654 bloodstream forms of pleomorphic *Trypanosoma brucei* strains in axenic culture.
1655 *Molecular and biochemical parasitology* **82**, 91-105 (1996).
- 1656 89 Wirtz, E., Leal, S., Ochatt, C. & Cross, G. A. A tightly regulated inducible expression
1657 system for conditional gene knock-outs and dominant-negative genetics in
1658 *Trypanosoma brucei*. *Molecular and biochemical parasitology* **99**, 89-101 (1999).
- 1659 90 Brun, R. & Schönenberger. Cultivation and in vitro cloning or procyclic culture forms
1660 of *Trypanosoma brucei* in a semi-defined medium. Short communication. *Acta tropica*
1661 **36**, 289-292 (1979).
- 1662 91 Wargnies, M. *et al.* Gluconeogenesis is essential for trypanosome development in the
1663 tsetse fly vector. *PLOS Pathogens* **14**, e1007502, doi:10.1371/journal.ppat.1007502
1664 (2018).
- 1665 92 Cross, M. *et al.* J-binding protein increases the level and retention of the unusual
1666 base J in trypanosome DNA. *Molecular microbiology* **46**, 37-47 (2002).
- 1667 93 Schumann Burkard, G., Jutzi, P. & Roditi, I. Genome-wide RNAi screens in
1668 bloodstream form trypanosomes identify drug transporters. *Molecular and*
1669 *biochemical parasitology* **175**, 91-94, doi:10.1016/j.molbiopara.2010.09.002 (2011).

- 1670 94 Kelly, S. *et al.* Functional genomics in *Trypanosoma brucei*: a collection of vectors for
1671 the expression of tagged proteins from endogenous and ectopic gene loci. *Molecular*
1672 *and biochemical parasitology* **154**, 103-109, doi:10.1016/j.molbiopara.2007.03.012
1673 (2007).
- 1674 95 Alibu, V. P., Storm, L., Haile, S., Clayton, C. & Horn, D. A doubly inducible system for
1675 RNA interference and rapid RNAi plasmid construction in *Trypanosoma brucei*.
1676 *Molecular and biochemical parasitology* **139**, 75-82,
1677 doi:10.1016/j.molbiopara.2004.10.002 (2005).
- 1678 96 Martins, G., Giacomelli, G., Goldbeck, O., Seibold, G. & Bramkamp, M. Substrate -
1679 dependent cluster density dynamics of *Corynebacterium glutamicum*
1680 phosphotransferase system permeases. *Molecular microbiology* **111**,
1681 doi:10.1111/mmi.14224 (2019).
- 1682 97 Dean, S. *et al.* A toolkit enabling efficient, scalable and reproducible gene tagging in
1683 trypanosomatids. *Open biology* **5**, 140197-140197, doi:10.1098/rsob.140197 (2015).
- 1684 98 Böhm, K. *et al.* Chromosome organization by a conserved condensin-ParB system in
1685 the actinobacterium *Corynebacterium glutamicum*. *bioRxiv*, 649749,
1686 doi:10.1101/649749 (2019).
- 1687 99 Kong, H. V. *et al.* A VSG expression site-associated gene confers resistance to
1688 human serum in *Trypanosoma rhodesiense*. *Cell* **95**, 839-846 (1998).
- 1689 100 Oberholzer, M., Morand, S., Kunz, S. & Seebeck, T. A vector series for rapid PCR-
1690 mediated C-terminal in situ tagging of *Trypanosoma brucei* genes. *Molecular and*
1691 *biochemical parasitology* **145**, 117-120, doi:10.1016/j.molbiopara.2005.09.002
1692 (2006).
- 1693 101 Salomon, Y. Adenylate cyclase assay. *Adv Cyclic Nucleotide Res* **10**, 35-55 (1979).
- 1694 102 Meijering, E., Dzyubachyk, O. & Smal, I. Methods for cell and particle tracking.
1695 *Methods in enzymology* **504**, 183-200, doi:10.1016/b978-0-12-391857-4.00009-4
1696 (2012).

- 1697 103 Rotureau, B. *et al.* Flagellar adhesion in *Trypanosoma brucei* relies on interactions
1698 between different skeletal structures in the flagellum and cell body. *Journal of cell
1699 science* **127**, 204-215, doi:10.1242/jcs.136424 (2014).
- 1700 104 Olmsted, J. B. Affinity purification of antibodies from diazotized paper blots of
1701 heterogeneous protein samples. *The Journal of biological chemistry* **256**, 11955-
1702 11957 (1981).
- 1703 105 Kohl, L., Sherwin, T. & Gull, K. Assembly of the paraflagellar rod and the flagellum
1704 attachment zone complex during the *Trypanosoma brucei* cell cycle. *The Journal of
1705 eukaryotic microbiology* **46**, 105-109 (1999).
- 1706 106 Bastin, P., Bagherzadeh, Z., Matthews, K. R. & Gull, K. A novel epitope tag system to
1707 study protein targeting and organelle biogenesis in *Trypanosoma brucei*. *Molecular
1708 and biochemical parasitology* **77**, 235-239 (1996).
- 1709 107 Dean, S., Marchetti, R., Kirk, K. & Matthews, K. R. A surface transporter family
1710 conveys the trypanosome differentiation signal. *Nature* **459**, 213-217,
1711 doi:10.1038/nature07997 (2009).
- 1712 108 Schindelin, J. *et al.* Fiji: an open-source platform for biological-image analysis. *Nature
1713 methods* **9**, 676-682, doi:10.1038/nmeth.2019 (2012).
- 1714 109 Schneider, C. A., Rasband, W. S. & Eliceiri, K. W. NIH Image to ImageJ: 25 years of
1715 image analysis. *Nature methods* **9**, 671-675 (2012).
- 1716 110 Dacheux, D. *et al.* A MAP6-related protein is present in protozoa and is involved in
1717 flagellum motility. *PLoS one* **7**, e31344-e31344, doi:10.1371/journal.pone.0031344
1718 (2012).
- 1719 111 Giroud, C. *et al.* Murine Models for *Trypanosoma brucei* gambiense disease
1720 progression--from silent to chronic infections and early brain tropism. *PLoS Negl Trop
1721 Dis* **3**, e509-e509, doi:10.1371/journal.pntd.0000509 (2009).
- 1722 112 Adler, J. & Parmryd, I. Quantifying colocalization by correlation: the Pearson
1723 correlation coefficient is superior to the Mander's overlap coefficient. *Cytometry. Part
1724 A : the journal of the International Society for Analytical Cytology* **77**, 733-742,
1725 doi:10.1002/cyto.a.20896 (2010).

- 1726 113 Zinchuk, V. & Zinchuk, O. Quantitative colocalization analysis of confocal
1727 fluorescence microscopy images. *Current protocols in cell biology Chapter 4*, Unit
1728 4.19, doi:10.1002/0471143030.cb0419s39 (2008).
- 1729 114 Stockmar, I. *et al.* Optimization of sample preparation and green color imaging using
1730 the mNeonGreen fluorescent protein in bacterial cells for photoactivated localization
1731 microscopy. *Scientific reports* **8**, 10137, doi:10.1038/s41598-018-28472-0 (2018).
- 1732 115 Baddeley, A., Rubak, E. & Turner, R. *Spatial Point Patterns: Methodology and*
1733 *Applications with R.* (Chapman and Hall/CRC, 2015).
- 1734 116 Cox, J. & Mann, M. MaxQuant enables high peptide identification rates, individualized
1735 p.p.b.-range mass accuracies and proteome-wide protein quantification. *Nature*
1736 *biotechnology* **26**, 1367-1372, doi:10.1038/nbt.1511 (2008).
- 1737 117 Tyanova, S., Temu, T. & Sinitcyn, P. The Perseus computational platform for
1738 comprehensive analysis of (prote)omics data. *13*, 731-740, doi:10.1038/nmeth.3901
1739 (2016).
- 1740 118 Vizcaíno, J. A. *et al.* ProteomeXchange provides globally coordinated proteomics
1741 data submission and dissemination. *Nature biotechnology* **32**, 223-226,
1742 doi:10.1038/nbt.2839 (2014).
- 1743 119 Vizcaíno, J. A. *et al.* 2016 update of the PRIDE database and its related tools.
1744 *Nucleic Acids Research* **44**, D447-D456, doi:10.1093/nar/gkv1145 %J Nucleic Acids
1745 Research (2015).
- 1746 120 Morriswood, B. *et al.* Novel bilobe components in *Trypanosoma brucei* identified
1747 using proximity-dependent biotinylation. *Eukaryot Cell* **12**, 356-367,
1748 doi:10.1128/ec.00326-12 (2013).
- 1749 121 Humphrey, S. J., Karayel, O., James, D. E. & Mann, M. High-throughput and high-
1750 sensitivity phosphoproteomics with the EasyPhos platform. *Nature protocols* **13**,
1751 1897-1916, doi:10.1038/s41596-018-0014-9 (2018).
- 1752 122 Rotureau, B., Subota, I., Buisson, J. & Bastin, P. A new asymmetric division
1753 contributes to the continuous production of infective trypanosomes in the tsetse fly.

- 1754 *Development (Cambridge, England)* **139**, 1842-1850, doi:10.1242/dev.072611
- 1755 (2012).
- 1756 123 Caljon, G. *et al.* The Dermis as a Delivery Site of *Trypanosoma brucei* for Tsetse
- 1757 Flies. *PLoS pathogens* **12**, e1005744-e1005744, doi:10.1371/journal.ppat.1005744
- 1758 (2016).
- 1759 124 Mirdita, M., Ovchinnikov, S. & Steinegger, M. ColabFold - Making protein folding
- 1760 accessible to all. *bioRxiv*, 2021.2008.2015.456425, doi:10.1101/2021.08.15.456425
- 1761 (2021).
- 1762 125 Schenk, R., Bachmaier, S., Bringaud, F. & Boshart, M. Efficient flavinylation of
- 1763 glycosomal fumarate reductase by its own ApbE domain in *Trypanosoma brucei*. *The*
- 1764 *FEBS Journal* **n/a**, doi:<https://doi.org/10.1111/febs.15812> (2021).
- 1765
- 1766

1767 **Acknowledgements**

1768 We thank Samuel Dean, Jessica Street and George Githure for plasmids,
1769 Nicolai Kolev, Frederic Bringaud, Keith Matthews and Melanie Bonhivers for
1770 antibodies, and Frank Schwede (Biolog, Bremen) for cAMP beads. We thank
1771 Benoit Vanhollebeke and David Pérez Morga for facilities for AC assay and
1772 HEK cell experiments (ULB, IBBM), Harry de Koning and Daniel Tagoe for
1773 exchange of information and Aline Crouzols and Robin Schenk for research
1774 assistance.

1775 The work was supported by a BioNa young scientists award of LMU to S.B.,
1776 MC-IEF Fellowship PIEF-GA-2013-626034 to M.K.G., IN.WBI excellence
1777 fellowship to L.R.V., CNPq/Universal Grant 725 422022/2016-0 to D.S. and
1778 LMU core funding to M.Bo. Work on super-resolution imaging was supported
1779 by grants from the Deutsche Forschungsgemeinschaft (DFG, grant numbers
1780 268759902 and 443931024) to M.Br. B.R. was supported by the Institut
1781 Pasteur, the Institut National pour la Santé et le Recherche Médicale
1782 (INSERM), the French Government Investissement d'Avenir programme -
1783 Laboratoire d'Excellence "Integrative Biology of Emerging Infectious
1784 Diseases" (ANR-10-LABX-62-IBEID) and the French National Agency for
1785 Scientific Research (projects ANR-14-CE14-0019-01 EnTrypa and ANR-18-
1786 CE15-0012 TrypaDerm).

1787

1788

1789

1790

1791 **Author Contributions**

1792 S.B., B.R., D.S., J.V.D.A., M.Br., and M.Bo. designed and supervised
1793 research; S.B., E.C.-A., G.G., L.R.V., E.L., A.A., M.K.G., J.V.D.A., A.B.
1794 performed research; J-W.D., I.F., A.I. performed, analysed or supervised
1795 mass spectrometry; S.B., G.G., E.C.-A., L.R.V., A.A., E.L., B.R., M.Br., D.S.,
1796 J.V.D.A., M.Bo. analyzed data; S.B. and M.Bo. wrote the paper.

1797

1798

1799 **Conflict of interest statement**

1800 The authors declare no competing interests.

1801

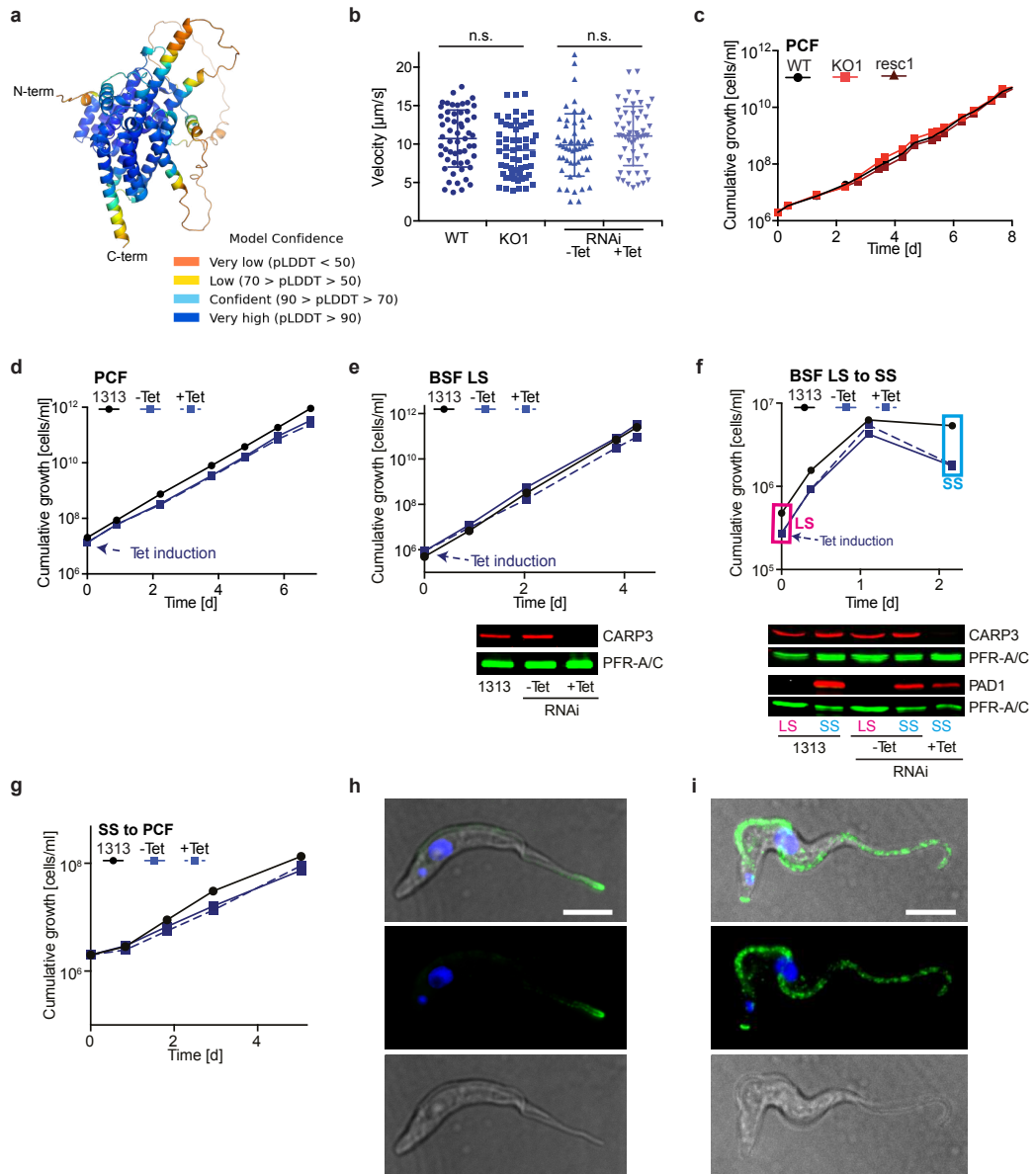
1802

1803 **Additional Information**

1804

1805 **Extended Data**

1806



Extended Data Fig. 1 CARP3 is not essential for growth or differentiation of *T. brucei* but shows life cycle stage-specific localization

a, Cartoon representation of a predicted model of *T. brucei* CARP3 using AlphaFold³⁷. Model confidence is illustrated using the predicted local-distance difference test ($p\text{LDDT}$) score, indicated by the color-coding.

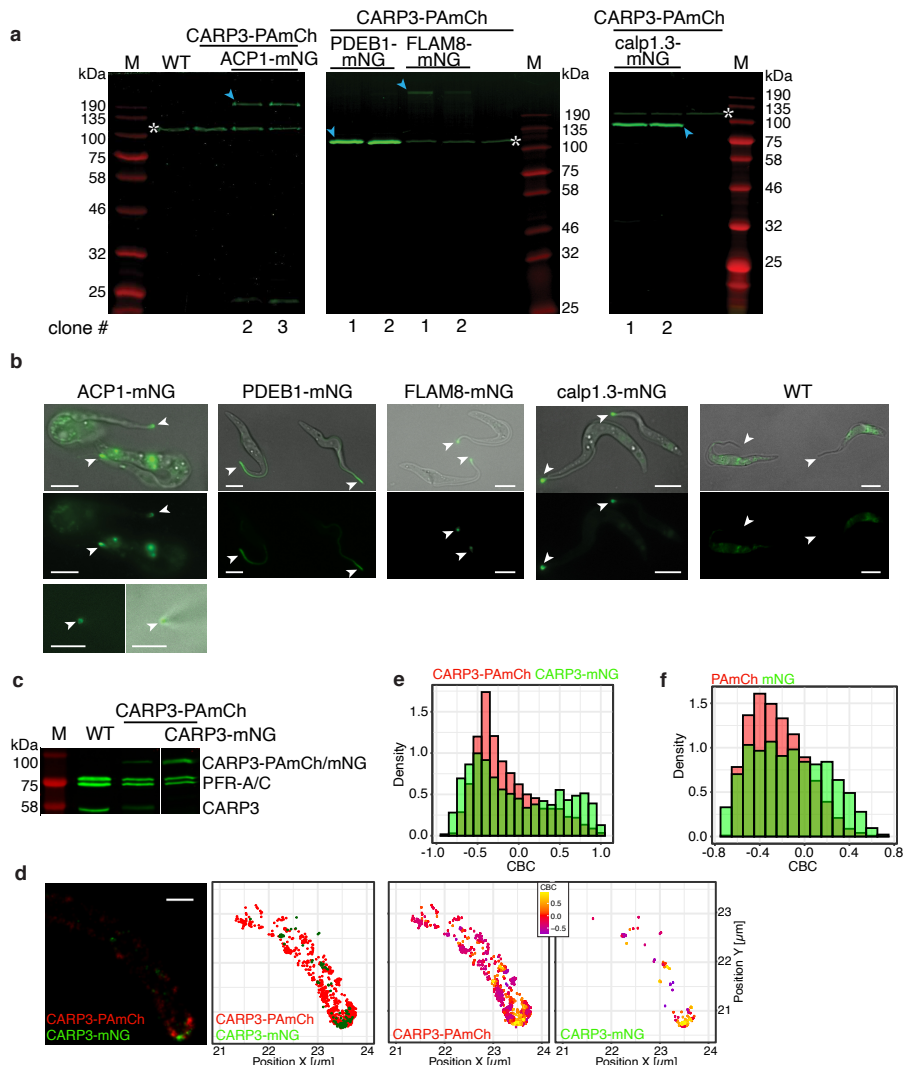
b, Analysis of single cell mean velocity (mean \pm SD; n = 56 (WT), 57 (KO1), 53 (RNAi -Tet), 54 (RNAi +Tet)) of procyclic form (PCF) AnTat 1.1 WT, *carp3* KO and RNAi cell lines. n.s.: non-significant ($p > 0.05$; ANOVA).

c, Representative growth curves of PCF AnTat 1.1 WT, *carp3* KO (KO1) and *CARP3* rescue (resc1) cell lines. Corresponding Western blot is shown in Fig. 1a.

d, e, Representative growth curves of PCF (d) or bloodstream form (BSF) (e) AnTat 1.1 1313 and tetracycline-inducible *CARP3* RNAi cell lines. RNAi was induced by addition of 5 $\mu\text{g}/\text{mL}$ tetracycline (+Tet condition). Repression of CARP3 levels was confirmed by Western blot analysis (e) with PFR-A/C as loading control. Western blot corresponding to (d) is shown in Fig. 1b.

f, g, Growth of cell lines as in (d, e) during differentiation from BSF long slender (LS) to short stumpy (SS) (f) or during SS to PCF differentiation (g). Western blot in (f) shows expression of CARP3 and the stumpy marker protein PAD1. PFR-A/C serves as loading control. The growth curve in (f) was started at time point 0 h with long slender cells at a density of 5.8×10^6 cells/mL and Tet induction of *CARP3* RNAi. Growth was monitored over 52 h without culture dilution, resulting in development into PAD1-expressing short stumpy forms. The growth curve in (g) was initiated with the SS cells from (f).

h, i, Indirect immunofluorescence analysis of CARP3 (green) in *T. brucei* AnTat 1.1 procyclic forms (h) or long slender bloodstream forms (i). DNA was stained with DAPI (blue). Fluorescence channels were merged with the differential interference contrast (DIC). Scale bars 5 μm .

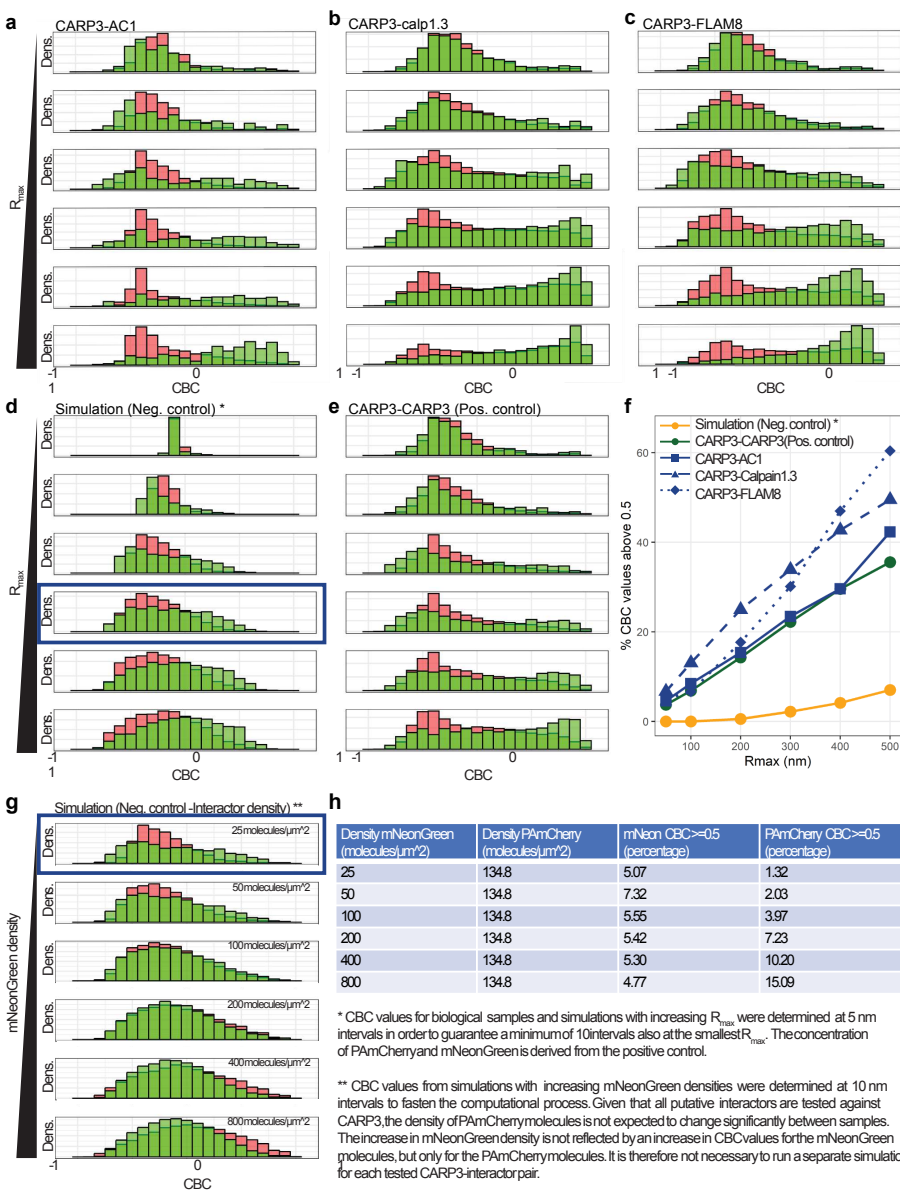


Extended Data Fig. 2 Generation of trypanosome cell lines for photoactivated localization microscopy of CARP3 and putative colocalization partners.

a, In-gel fluorescence and **b**, live cell fluorescence microscopy of procyclic *T. brucei* AnTat 1.1E expressing CARP3-PAmCh (PAmCh) and ACP1P, PDEB1, FLAM8, or calpain 1.3 (calp1.3), respectively, C-terminally fused to mNeonGreen (mNG) (labeled by blue arrowheads in (a)). Wild type (WT) cells were included as control. The white asterisk (*) marks an endogenous, autofluorescent protein that we identified as fumarate reductase¹²⁴. Note that the PDEB1-mNG fusion protein runs at the same apparent molecular weight as the autofluorescent fumarate reductase. White arrowheads in (b) point towards flagellar tips. The second image shown for ACP1-mNG displays a fluorescent flagellar tip from the top perspective. Scale bars 5 μ m. M protein molecular weight marker.

c, Western blot analysis (anti-CARP3, anti-PFR-A/C (loading control)), **d**, PALM imaging and **e**, colocalization analysis (as in Fig. 2) of procyclic *T. brucei* AnTat 1.1E expressing CARP3-PAmCherry (PAmCh, red) and CARP3-mNeonGreen (mNG, green). While WT cells express CARP3 (~57 kDa) from two endogenous alleles (c, lane 'WT'), the hemizygous *in situ* CARP3-PAmCherry cells (middle lane in (c)) express CARP3 from one wild type allele (~57 kDa) and one endogenous CARP3-PAmCherry fusion (~85 kDa). The CARP3-PAmCherry/CARP3-mNG (c, right lane) cell line expresses two endogenously tagged CARP3 alleles, both resulting in proteins with similar molecular weight (~85 kDa), one fused to PAmCherry, the other fused to mNG, resulting in replacement of both endogenous alleles. Scale bar in (d) 0.5 μ m.

f, CBC values distributions for two simulated independent Poisson point patterns characterized by densities equal to the ones from procyclic *T. brucei* AnTat 1.1E expressing CARP3-PAmCherry and CARP3-mNeonGreen. The point patterns are confined within a rectangular area of 1 μ m width (approximation of a straight flagellum).



Extended Data Fig. 3 Coordinate-based colocalization (CBC) analysis of PALM data for CARP3 and putative colocalization partners.

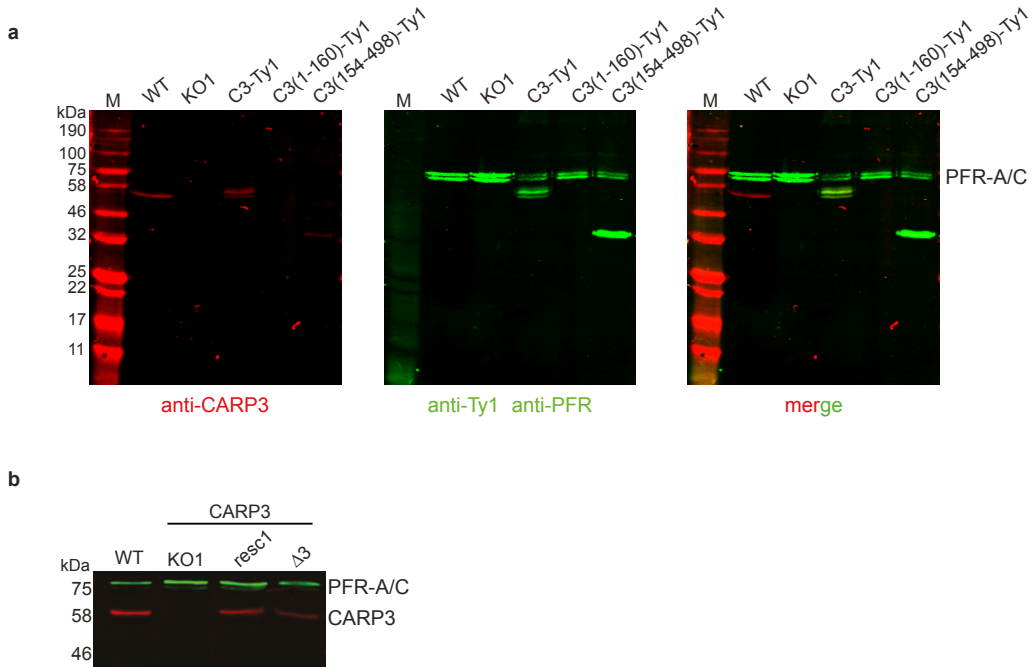
a-e, CBC value density distributions for CARP3-AC1 (a), CARP3-calpain 1.3 (b), CARP3-FLAM8 (c), negative control (d) and CARP3-CARP3 (e) calculated for six different R_{\max} (50, 100, 200, 300, 400, 500 nm). The CBC value density distributions for mNeonGreen-tagged proteins relative to PAmCherry-tagged proteins is shown in green, while the opposite is shown in red. Interval width = 5 nm.

f, The percentage of CBC values above or equal to 0.5 relative to R_{\max} derived from (a-e) is plotted for each fluorescent protein pair and compared to the positive and the negative control.

g, h, CBC value density distributions calculated for simulations characterized by increasing mNeonGreen concentrations (25, 50, 100, 200, 400 and 800 molecules/μ²) and constant PAmCherry concentration (g). $R_{\max} = 300$ nm, interval width = 10 nm. The percentage of CBC values above or equal to 0.5 (mNeonGreen to PAmCherry and vice versa) was determined and compared for all mNeonGreen densities to evaluate the necessity of separate negative controls for each protein pair (h).

1810

1811



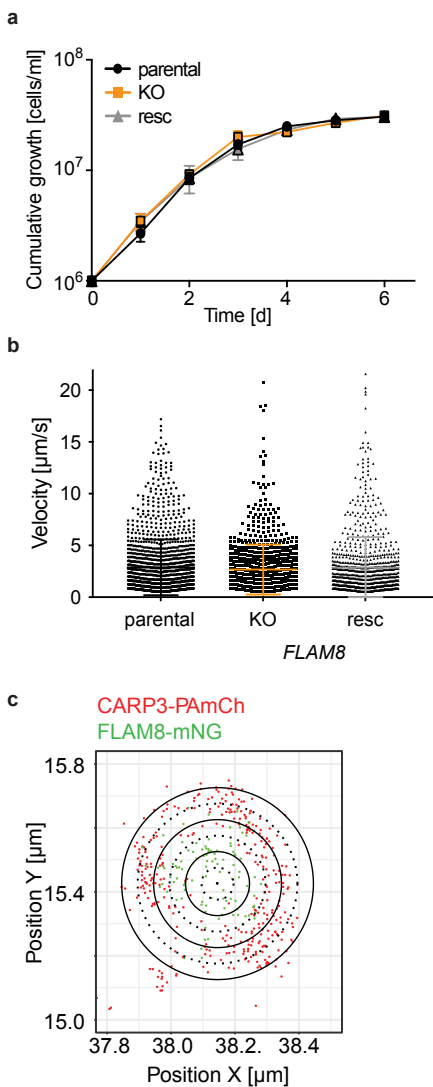
Extended Data Fig. 4 Expression of CARP3 mutant proteins

a, Western blot analysis of procyclic *T. brucei* AnTat 1.1 constitutively overexpressing CARP3-Ty1, CARP3(1-160)-Ty1 or CARP3(154-498)-Ty1 or **b**, *in situ* rescue with full-length CARP3 (resc1) or CARP3 Δ 3 (Δ 3) in a carp3 knock out (KO) background. Wild type (WT) and KO (KO1) cell lines were included as controls. Western blots were probed with anti-CARP3, anti-Ty1 (only in (a)) and anti-PFR-A/C (loading control).

Note that CARP3(1-160)-Ty1 (calculated molecular weight 19.5 kDa) is not detectable by Western blot but only by immunofluorescence microscopy (see Fig. 2k). M: protein molecular weight marker.

1812

1813



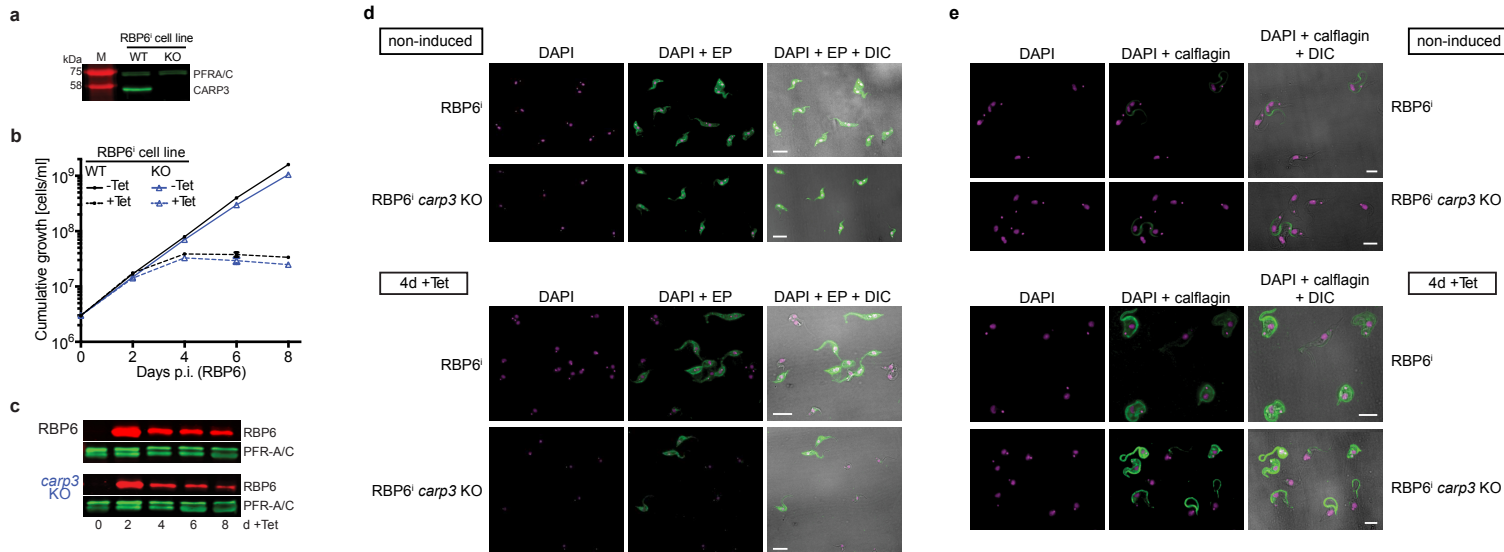
Extended Data Fig. 5 *FLAM8* knock out cells have no growth or motility phenotype

a, b, Representative growth curves (**a**) and analysis of single cell mean velocity (**b**) of AnTat 1.1E ‘Paris’ parental, *flam8* knock out (KO) or *FLAM8* rescue (resc) expressing the red triple marker. (**b**) shows mean \pm SD of $n = 1502$ (parental); $n = 898$ (KO); $n = 898$ (resc).

c, Single molecule localization of CARP3-PAmCherry and FLAM8-mNG from Fig. 3e shown via centroids. Rings are drawn in 50 nm steps from center of flagellar tip cross-section. Dotted lines 50 nm, solid lines 100 nm.

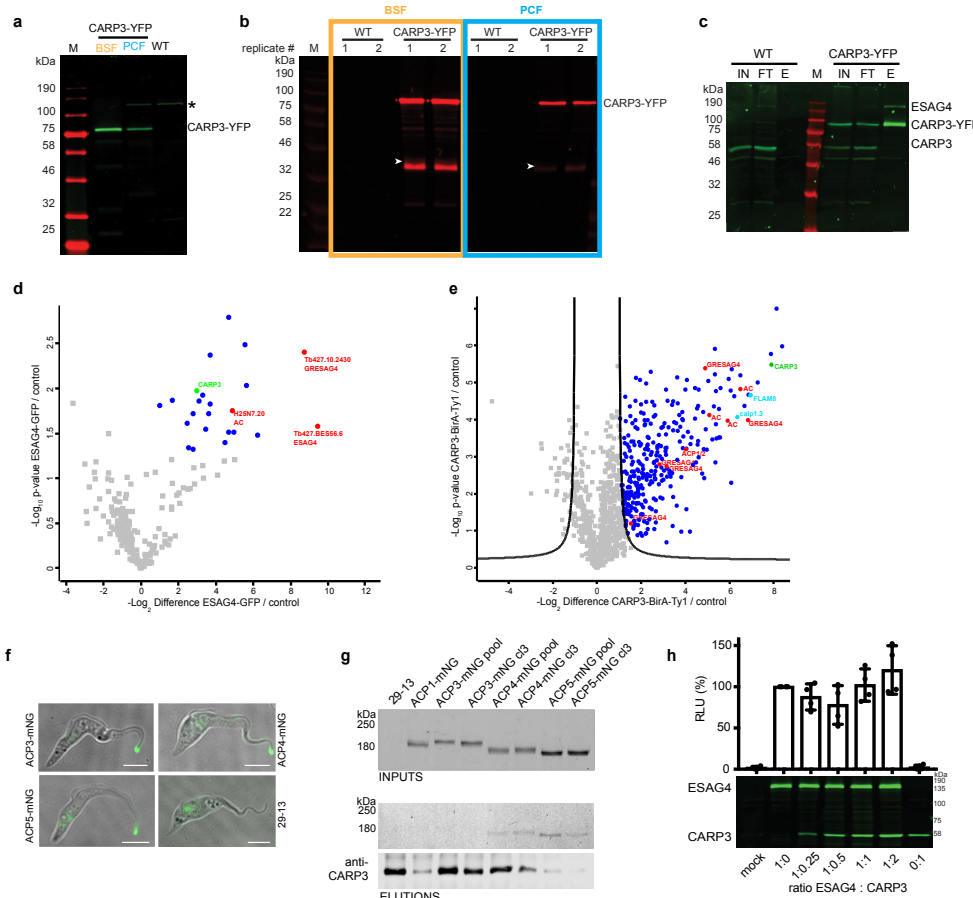
1814

1815



Extended Data Fig. 6 *CARP3* KO parasites are fully differentiation-competent in the *in vitro* RBP6 overexpression system

- a, Western blot analysis of CARP3 expression in a homozygous deletion mutant of *carp3* (KO) generated in a procyclic *T. brucei* EATRO 1125 cell line allowing (Tet)-inducible RBP6 overexpression (RBP6'). PFR-A/C serves as loading control.
- b, c, Cumulative growth (b) and Western blot (c) analyses of cell lines as in (a) with or without Tet induction (10 µg/mL) of RBP6 overexpression. Growth curves are mean ± SD of n = 3 for +Tet; n = 1 for -Tet. Western blots show inducible overexpression of RBP6 for both cell lines. PFR-A/C serves as loading control.
- d, e, Indirect immunofluorescence analysis of EP procyclin (d) or calflagin (e) in the cell lines indicated. Marker protein expression was analyzed before (non-induced; upper panels) and four days after induction of RBP6 expression with 10 µg/mL tetracycline (4d +Tet; lower panels). DNA was stained with DAPI (magenta). Scale bars 5 µm.



Extended Data Fig. 7 CARP3 interacts with ACs and regulates their abundance

a, In-gel fluorescence of *T. brucei* BSFs and PCFs of strain AnTat 1.1E expressing CARP3-YFP *in situ*. Procytic wild type cells (WT) were loaded as control. The asterisk (*) marks an autofluorescent fumarate reductase¹²⁴.

b, GFP trap pull-down of cell lines from (a). The Western blot probed with anti-CARP3 shows the eluted fractions of two replicates each. The band at ~35 kDa (white arrowhead) is probably a proteolytic degradation product of CARP3.

c, GFP trap pull-down in *T. brucei* MiTat 1.2 BSF wild type (WT) or CARP3-YFP cells. The Western blot was probed with anti-CARP3 and anti-ESAG4. IN input; FT flow-through; E elution.

d, GFP trap pull-down in *T. brucei* MiTat 1.2 BSF 13-90 (control) or derived ESAG4-GFP expressing cells. The in-gel fluorescence analysis shows expression and solubility of ESAG4-GFP upon detergent lysis in the input fraction and pull-down of ESAG4-GFP in the eluted fraction. The Volcano plot displays proteins plotted according to p-value and fold change derived from mass spectrometry analysis of two replicate pull-downs. Significantly enriched proteins (ESAG4-GFP / control) ($p\text{-value} \leq 0.05$) are represented by blue dots. AC isoforms are shown in red, CARP3 in green.

e, CARP3 proximity proteomics using BiOLD. Volcano plot representation of CARP3 BiOLD comparing pull-down of biotinylated proteins from BSF *T. brucei* Δ carp3/CARP3-BirA*-Ty1 versus Δ carp3/CARP3. Proteins are plotted according to p-value and fold change. Significantly enriched proteins (CARP3-BirA*-Ty1 / control) ($p\text{-value} \leq 0.05$, $s_0=2$) are represented by blue dots and localize above the significance line on the right. CARP3: green; FLAM8 and calpain 1.3: cyan; AC isoforms: red.

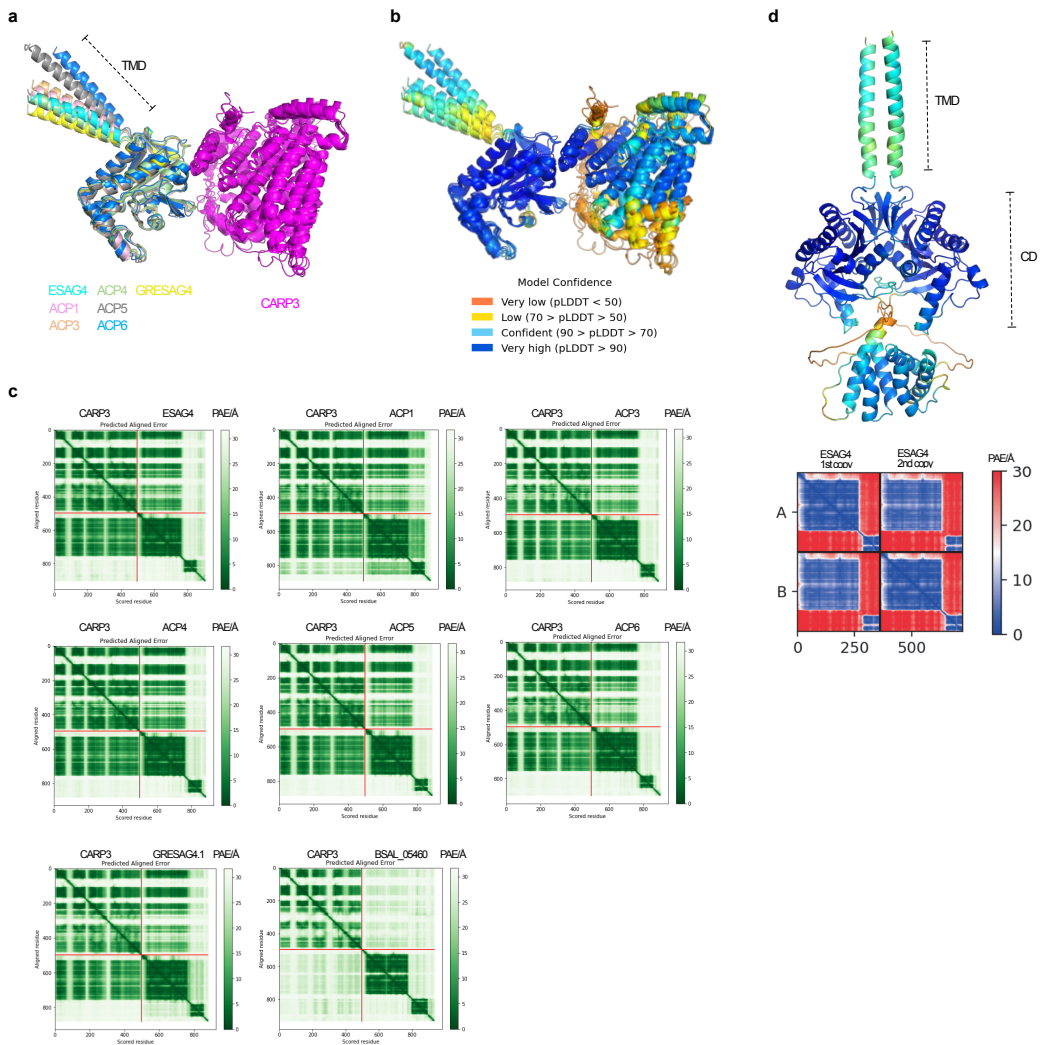
f, Fluorescence microscopy of procyclic *T. brucei* 29-13 and derived ACP3-, ACP4- or ACP5-mNeonGreen expressing cells. Scale bars 5 μ m.

g, CARP3 IP in procyclic *T. brucei* 29-13 and derived ACP1-, ACP3-, ACP4- or ACP5-mNeonGreen expressing cell lines. Upper panel: in-gel fluorescence analysis of ACP-mNG in input fractions (INPUTS). Lower panels: in-gel fluorescence analysis of ACP-mNG and Western blot detection of CARP3 in eluted fractions (ELUTIONS).

h, Dual-Luciferase® cAMP reporter assay in HEK cells transfected with ESAG4 and CARP3 expression vectors at the indicated ratios. Equal amounts of total DNA were transfected in all conditions. Relative light units (RLU) of the dual-luciferase assay were normalized to ESAG4 protein levels with one representative Western blot (anti-CARP3, anti-ESAG4) shown. The RLU value for the 1:0 ratio of ESAG4:CARP3 was set to 100%. The graph shows mean \pm SD of four independent biological replicates.

1817

1818



Extended Data Fig. 8 Structure modeling of CARP3-AC complexes using AlphaFold

a. Cartoon representation of seven AlphaFold-generated models of CARP3 (magenta) in complex with the intracellular catalytic domain of different ACs (each AC isoform is shown by a different color, as indicated; ESAG4: Tb427.BES40.13; ACP1: Tb927.11.17040; ACP3: Tb927.7.7470; ACP4: Tb927.10.13040; ACP5: Tb927.11.13740; ACP6: Tb927.9.15660; GRESAG4.1: Tb927.6.760). The transmembrane domain (TMD) of the receptor-type ACs is labeled. The AC extracellular N-terminal part was not included in the structure prediction. The models are shown after superpositioning of CARP3.

b. Same as panel (a) but colored according to local model confidence using the predicted local-distance difference test (pLDDT) score.

c. Predicted alignment error (PAE) plots for the models shown in panels (a, b), indicating the confidence of the complex modelling. The PAE for the predicted model of *T. brucei* CARP3 in complex with a receptor-type transmembrane AC (BSAL_05460) from the distantly related kinetoplastid *Bodo saltans* that lacks a CARP3 orthologue was included as a negative control.

d. AlphaFold-generated model for an ESAG4 AC homo-dimer (ESAG4 amino acids 862-end, lacking the extracellular N-terminal part) color-coded according to pLDDT score. TMD transmembrane domain; CD catalytic domain.

1820 **Supplementary Data**

1821

1822 **Supplementary Fig. 1 Expression or localization of CARP3 is not**
1823 **dependent on intracellular cAMP levels**

1824 **a**, Pull-down assay using cAMP-coupled agarose beads (2-AHA or 8-AHA
1825 linker) and lysate of *T. brucei* AnTat 1.1E expressing PDEB1-mNeonGreen
1826 (PDEB1-mNG). PDEB1- mNG serves as positive control for cAMP binding
1827 and was detected by in-gel fluorescence; CARP3 was detected by
1828 immunoblotting using rabbit anti-CARP3. Lanes represent input material (I),
1829 flow-through (FT), washes (W) and eluted material (E).

1830 **b**, Fluorescence microscopy of CARP3-YFP (green) in procyclic *T. brucei*
1831 AnTat 1.1E in the presence (24h, 48h) or absence (control) of 1 μ M CpdA or
1832 CpdB for 24 h or 48 h, respectively. Scale bars 5 μ m.

1833 **c**, Social motility assay of CpdA- or CpdB-treated (1 μ M) or untreated cells as
1834 in (b).

1835

1836 **Supplementary Table 1. Summary of coordinate-based colocalization**
1837 **(CBC) analysis.**

1838

1839 **Supplementary Table 2. CARP3-YFP pull-down in bloodstream forms**
1840 **(2a) or procyclic forms (2b).**

1841

1842 **Supplementary Table 3. ESAG4-GFP pull-down in bloodstream forms.**

1843

1844 **Supplementary Table 4: CARP3 Bioid proximity proteomics identifies**

1845 **putative CARP3 interactors.**

1846

1847 **Supplementary Table 5. Quantitative proteomics upon CARP3 knock**

1848 **down.**

1849

1850 **Supplementary Table 6: Summary of AC isoforms identified by proteome**

1851 **studies in Supplementary Tables 2, 4 and 5.**

1852

1853 **Supplementary Table 7: List of Primers used for cloning.**

1854

Supplementary Files

This is a list of supplementary files associated with this preprint. Click to download.

- [SuppTable1.xlsx](#)
- [SuppTable2.xlsx](#)
- [SuppTable3.xlsx](#)
- [SuppTable4.xlsx](#)
- [SuppTable5.xlsx](#)
- [SuppTable6.xlsx](#)
- [SuppTable7.xlsx](#)
- [SupplementaryFig1.pdf](#)
- [PDBExtendedDataFig.8a.txt](#)
- [PDBExtendedDataFig.8d.txt](#)
- [pymolExtendedDataFig.8a.pse](#)
- [pymolExtendedDataFig.8d.pse](#)